UCLA
UCLA Previously Published Works

Title

Ocean convective available potential energy. Part II: Energetics of Thermobaric Convection and Thermobaric Cabbeling

Permalink

Journal

ISSN

Authors

Su, Z
Ingersoll, AP
Stewart, AL
et al.

Publication Date

DOI

Peer reviewed

Ocean Convective Available Potential Energy. Part II: Energetics of Thermobaric Convection and Thermobaric Cabbeling

Zhan Su * and Andrew P. Ingersoll

Division of Geological and Planetary Sciences, California Institute of Technology, Pasadena, California

Andrew L. Stewart

Department of Atmospheric and Oceanic Sciences, University of California, Los Angeles, California

Andrew F. Thompson

Environmental Science and Engineering, California Institute of Technology, Pasadena, California

ABSTRACT

We investigate the energetics of thermobaricity- and cabbeling-powered deep convection occurring in oceans with cold fresh water overlying warm salty water. These quasi-two-layer profiles are widely observed in wintertime polar oceans. Our key diagnostic is Ocean Convective Available Potential Energy (OCAPE), a concept introduced in Su et al. (2015). For an isolated ocean column, OCAPE arises from thermobaricity and is the maximum potential energy (PE) that can be converted into kinetic energy (KE) under adiabatic vertical parcel rearrangements. We explore the KE budget of convection using two-dimensional numerical simulations and analytical estimates. We find that OCAPE is a principal source for KE. However, the complete conversion of OCAPE to KE is inhibited by diabatic processes. Further, we find that diabatic processes produce three other distinct contributions to the KE budget: (i) A sink of KE due to the reduction of stratification by vertical mixing, which raises water column's center of mass and thus converts KE to PE; (ii) A source of KE due to cabbeling-induced shrinking of water column's volume when water masses with different temperatures are mixed, which lowers the water column's center of mass and thus converts PE into KE; (iii) a reduced production of KE due to diabatic energy conversion of the KE-convertible part of the PE to the KE-inconvertible part of the PE. Under some simplifying assumptions, we propose a strategy to estimate the maximum depth of convection from an energetic perspective. This study provides a potential basis for improving the convection parameterization in ocean models.

1. Introduction

Akitomo (1999a) classified ocean deep convection into two types: Type I is the deepening of the mixed layer in a relatively homogeneous ocean driven mainly by the loss of surface buoyancy. Type II is thermobaric convection, in which plumes of cold fresh water (CFW) sink into warm salty water (WSW) with significant modulation from thermobaricity and cabbeling (Garwood Jr et al. 1994; Akitomo 1999a,b; McPhee 2000; Ingersoll 2005; Adkins et al. 2005; Akitomo 2007). Harcourt (2005) was the first to simulate Type III convection, also called thermobaric cabbeling, in which convective plumes of CFW/WSW mixture sink into WSW due to cabbeling instability, and later accelerate further due to thermobaricity and cabbeling (see also the associated observation of Type III convection in an unpublished manuscript by Padman et al. 1998). Cabbeling instability is a convective phenomenon that occurs when water masses with different temperatures are mixed dia-

batically to produce a denser water mass than the parent waters (Carmack 1979). "Cabbeling" in this manuscript always means the quadratic dependency of water density on potential temperature (McDougall 1987).

In this paper, we focus on the energetics of Type II and Type III convection. But we do not distinguish between them: Their dynamics are both strongly influenced by thermobaricity and cabbeling (discussed more in section 6b) and they both occur in oceans with CFW overlying WSW. These quasi-two-layer stratifications are widely observed in winter-time polar oceans (Gordon and Huber 1990; Garwood Jr et al. 1994; McPhee 2000). These convection events rapidly transport heat vertically and may make substantial contributions to local vertical mixing, deep-water production, and open-ocean polynyas in polar regions (Akitomo 1999b; McPhee 2003; Harcourt 2005). However, these contributions are poorly understood due to the paucity of observations and the inability of large-scale ocean models to resolve convection (Denbo

1

and Skyllingstad 1996). In this paper and its companion (manuscript submitted to J. Phys. Oceanogr., hereinafter Part I; Su et al. 2015), we introduce a new diagnostic for thermobaricity, the Ocean Convective Available Potential Energy (OCAPE), to facilitate the analysis of these convection events.

OCAPE is conceptually important (Part I): it parallels atmospheric Convective Available Potential Energy (CAPE), a key energy source in atmospheric moist convection that has long been used to forecast moist convection (Arakawa and Schubert 1974; Emanuel et al. 1994; Trenberth 2005). Both OCAPE and CAPE measure the potential energy (PE) of a fluid column minus the PE of its reference (global minimum-PE) state that is achievable under adiabatic vertical parcel rearrangements. Here PE is the sum of the gravitational and internal energies. OCAPE arises from thermobaricity and it is computable following the algorithm in Part I. In principle, OCAPE can be entirely released into kinetic energy (KE) if the ocean column evolves adiabatically from the current state to the reference state (Part I). In this paper we simulate the release of OCAPE and find that diabatic processes inhibit this complete conversion of OCAPE to KE. We generalize the part of OCAPE that can be released to KE (S_{tb} below).

A central diagnostic quantity in our analysis is the cumulative KE production in a convection event, denoted as KE_{cum}, which measures the accumulated intensity of convective motions. At any instant, KE_{cum} is equal to the current KE plus the time-integrated viscous dissipation of KE up to that time (denoted as $Heat_{vis}$). In this study we pose a conceptual decomposition of KE_{cum} into four different contributions

$$KE_{cum} = KE + Heat_{vis} = S_{tb} - S_{strat} + S_{cab} - C_{H^D to H^P}. \tag{1}$$

Equation (1) gives a conceptual overview of the physics before getting into the details in the following sections. The physical nature of each term in (1) is explained by bullet points below, while its mathematical derivation is provided in Appendix A. This decomposition is derived for simplified equation of state (EOS) and initial stratification (CFW overlying WSW, as widely observed in winter-time polar oceans; see, *e.g.*, Gordon and Huber 1990), but for more general initial stratifications it does not hold exactly. The effectiveness of this decomposition is verified by its prediction of KE_{cum} and the maximum depth of convection that are in close agreement with numerical simulations presented in sections 3–5.

The energy terms/relations in (1), as introduced below, are summarized schematically in Figure 1. For an isolated system, KE+PE is constant by energy conservation. Thus the KE production is converted from PE. The PE of a system can be divided into two parts: dynamic enthalpy, H^D, and potential enthalpy, H^P (Young 2010; McDougall

2003); only PE stored in H^D is convertible to KE. We consider below conceptually how the four terms in Equation (1) are related to three energy reservoirs: KE, H^D and H^P.

- $C_{H^D to H^P}$, as detailed in section 4c and (15b), represents the time-integrated conversion of H^D to H^P due to diabatic processes. Thus the time-integrated conversion of H^D to KE, which is KE_{cum}, is equal to the state change of H^D (compared to the initial state) minus $C_{H^D to H^P}$. We derive in Appendix A that three sources/sinks contribute to the state change of H^D ($= KE_{cum} + C_{H^D to H^P}$) as follows.

- S_{tb}, as detailed in section 3a–3b and (21c), is a source of H^D that extracts energy from OCAPE.

- $-S_{strat}$ is a sink of H^D as detailed in section 3c and (20a). For an initially stably stratified ocean column ($N^2 > 0$), vertical mixing during convection reduces the stratification, which raises the water column's center of mass and thus converts KE into PE (H^D).

- S_{cab} is a source of H^D as detailed in section 4b and (25). When water masses with different temperatures (*i.e.* CFW and WSW) are mixed during convection, cabbeling reduces the water column's volume, which lowers the water column's center of mass and thus converts PE (H^D) into KE.

These four terms are not coupled but are independent of each other (see (A1) and (A10)-(A11) in Appendix A). $C_{H^D to H^P}$ is the process-based conversion between the energy reservoirs of H^D and H^P (Figure 1), totally determined by the full diabatic processes governed by the equation of motion (see (15b)). In other words, knowing only the initial (pre-convection) and the final (post-convection) states, but without knowing the processes for the transition, one cannot quantify $C_{H^D to H^P}$. In contrast, H^D is a thermodynamic function of the system: The change of H^D (and its three components: S_{tb}, $-S_{strat}$ and S_{cab}; see (A11) and Figure 1) due to convection are totally determined from the initial and the final states, despite the (unpredictable turbulent) diabatic processes that transform the initial state to the final state[1]. We also show that the final state can be determined *a priori* given the initial quasi-two-layer state (section 4e). S_{strat} and S_{cab} are also independent from each other: the latter is determined by the reduction of system's temperature variance during convection and is independent of N^2; the former is determined from the reduction of N^2. Note that S_{strat}, S_{cab} and $C_{H^D to H^P}$ will only be non-zero if diabatic processes occur. Adiabatic processes, which define OCAPE, affects S_{tb}

---

[1]Similarly, the change of gravitational potential energy of an object only depends on its initial and final heights, despite the numerous pathways (processes) that connect the initial and the final position.

(see (21b)). However, S_{tb} is also influenced by the diabatic processes since it is state-based.

In section 2 we derive the fundamentals of energy conservation and describe the numerical model. It would be very helpful for the reader to go through the fundamentals of thermodynamics in section 2 to better capture the main points of this study. In section 3, we isolate and explain S_{tb} and S_{strat} using simplified simulations (excluding cabbeling in the EOS). In section 4 we increase the complexity of our simulation (using the full EOS) to evaluate and explain S_{cab} and $C_{H^D to H^P}$. We further propose a strategy to predict the maximum depth of convection. In section 5, we apply this strategy and (1) to a convection event initially based on a realistic profile from Weddell Sea. Section 6 comprises our discussion and conclusions. Numerical experiments (Tables 1-5; Figures 2, 4, 5, 6, 7) in this manuscript is organized following step-by-step diagnosis for our energy decomposition, as stated by their titles.

2. Fundamentals for the energetics of Type II and Type III convection

a. Energy conservation, potential/dynamic enthalpy and model description

We introduce a Boussinesq model that conserves energy for an isolated system, which is key for our energy analysis. For computational efficiency the model is restricted to two dimensions: horizontal y and vertical z, with vertical velocity $w = -\partial\psi/\partial y$ and horizontal velocity $v = \partial\psi/\partial z$ defined via a streamfunction ψ. We neglect Coriolis accelerations (see section 6b for associated discussion). By taking the curl of the momentum equation, we obtain the vorticity equation

$$\frac{D\nabla^2\psi}{Dt} = -\frac{\partial b}{\partial y} + \nu\nabla^2\nabla^2\psi, \qquad (2)$$

where ν is the kinematic viscosity. More sophisticated schemes for turbulent viscosity (*e.g.*, Harcourt et al. 2002; Harcourt and D'Asaro 2008) could better parameterize subgrid turbulence. Here we adopt a Laplacian viscosity because it is convenient for enforcing energy conservation. In equation (2) we use the modified buoyancy of Young (2010):

$$b = b(\theta, S, P) \equiv b(\theta, S, z) = -g(\rho - \rho_0)/\rho, \qquad (3)$$

where θ, S, P and ρ_0 are potential temperature, salinity, pressure and constant reference density, respectively. Here we replace P with z following the hydrostatic relation under Boussinesq approximation (Young 2010). Following Equations (57.3) and (57.6) of Landau and Lifshitz (1959),

we have the salinity and thermodynamic equations

$$\frac{DS}{Dt} = -\frac{1}{\rho_0}\nabla \cdot \mathbf{i}, \qquad (4a)$$

$$T\frac{D\eta}{Dt} = \frac{1}{\rho_0}\left[-\nabla \cdot (\mathbf{q} - \mu\mathbf{i}) - \mathbf{i} \cdot \nabla\mu + \rho_0\nu(\nabla^2\psi)^2\right], \quad (4b)$$

where η is specific entropy, T is temperature, $\mathbf{i}$ is diffusive salt flux, $\mathbf{q}$ is diffusive energy flux, μ is the relative chemical potential of salt in seawater, and $\rho_0\nu(\nabla^2\psi)^2$ is viscous heating. Following $\eta = \eta(\theta, S)$ we rewrite (4b) as

$$T\frac{D\eta}{Dt} = C_p\frac{D\theta}{Dt} - T\mu_\theta\frac{DS}{Dt}, \qquad (5a)$$

$$C_p = T\frac{\partial\eta}{\partial\theta}\bigg|_S, \qquad -\mu_\theta = -\frac{\partial\mu}{\partial T}\bigg|_{S,P_r} = \frac{\partial\eta}{\partial S}\bigg|_\theta, \qquad (5b)$$

following Maxwell's relations. Here P_r is the reference pressure at sea level. Substituting (4a) into (5a) and using (4b), we obtain the evolution equation for θ

$$\frac{D\theta}{Dt} = -\frac{\nabla \cdot [\mathbf{q} - (\mu - T\mu_\theta)\mathbf{i}]}{C_p\rho_0} - \frac{\mathbf{i} \cdot \nabla(\mu - T\mu_\theta)}{C_p\rho_0} + \frac{\nu(\nabla^2\psi)^2}{C_p}. \qquad (6)$$

Note that C_p is proportional to T and is not a constant, as shown in (5b). Therefore viscous heating and diffusion lead to the non-conservation of θ, according to (6).

We demonstrate that equations (2), (3), (4a) and (6) (following Ingersoll 2005; Young 2010; Landau and Lifshitz 1959) compose a non-hydrostatic energy-conserving (NHEC) model. From Part I, PE can be represented by the system's enthalpy (the energy in this paper, if not otherwise stated, is always column-averaged and in units of J/kg):

$$\text{PE} = H = \frac{1}{\iint \rho_0 dy dz}\iint h\,\rho_0 dy dz, \qquad (7)$$

where h is specific enthalpy and has the following thermodynamic potential

$$\frac{\partial h}{\partial\theta}\bigg|_{S,P} = C_p, \qquad \frac{\partial h}{\partial S}\bigg|_{\theta,P} = \frac{\partial h}{\partial S}\bigg|_{\eta,P} + \frac{\partial h}{\partial\eta}\bigg|_{S,P}\frac{\partial\eta}{\partial S}\bigg|_\theta = \mu - T\mu_\theta. \qquad (8)$$

where we have applied $\partial h/\partial S|_{\eta,P} = \mu$, $\partial h/\partial\eta|_{S,P} = T$ and (5b). One derives the energy conservation by multiplying (2) by $-\rho_0\psi$, multiplying (6) by $\rho_0\partial h/\partial\theta$ as expressed in (8), multiplying (4a) by $\rho_0\partial h/\partial S$ as expressed in (8), and then adding the result and integrating:

$$\frac{\partial}{\partial t}(\text{KE} + H) = \frac{1}{\iint \rho_0 dy dz}\iint \left\{\rho_0\psi J(\psi, \nabla^2\psi) - \rho_0 J(\psi, h) - \nabla \cdot \mathbf{q}\right.$$
$$\left. + \rho_0\nabla \cdot \left[\nu\nabla^2\psi\nabla\psi - \nu\psi\nabla\nabla^2\psi\right]\right\} dy dz = 0, \qquad (9)$$
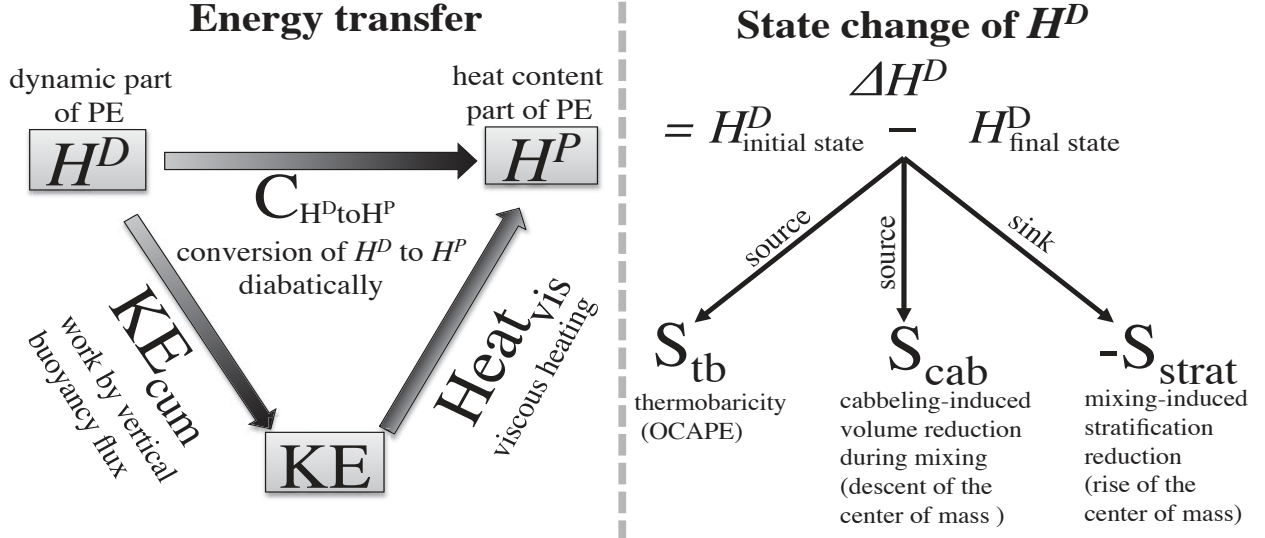
3

Energy transfer | **State change of H^D**

FIG. 1. Schematic of the proposed energetics for Type II and Type III convection. Definitions and denotations here follow section 2a. (left panel) Potential energy (PE) can be represented by the system's enthalpy H, which includes the dynamic part H^D and the heat content part H^P (defined in (11a)–(11d)). $C_{H^D toH^P}$ is the time-integrated energy transfer from the H^D reservoir to the H^P reservoir diabatically (defined in (15b)). Heat$_{vis}$ is the time-integrated viscous heating (defined in (15a)), which transfers energy from the KE reservoir to the H^P reservoir. KE$_{cum}$ is the time-integrated work done by vertical buoyancy flux (defined in (14b)), which transfers energy from the H^D reservoir to the KE reservoir. Thus KE$_{cum}$ equals the current KE plus Heat$_{vis}$, as well as equaling the state change of H^D minus $C_{H^D toH^P}$ (see (13b)). (right panel) The state change of H^D is due to three distinct sources/sinks: S$_{tb}$, S$_{cab}$, and $-$S$_{strat}$ (defined in (21b),(25),(20a), respectively). Therefore, KE$_{cum}$ has four contributions: $-$C$_{H^D toH^P}$, S$_{tb}$, S$_{cab}$, and $-$S$_{strat}$ (*i.e.* (1)). The mathematical derivation of Equation (1) is provided in Appendix A.

where J is the Jacobian. All terms on the right-hand side of (9) vanish provided there is no viscous stress, no normal velocity, and no diffusion of energy at/across the boundaries. In deriving the second term on the right-hand side of (9) we have applied $\partial h/\partial z|_{S,\theta} = -b$, $J(\psi,z) = w = -\partial\psi/\partial y$ and integration by parts. Therefore the energy conservation of (9) is independent of the form of $\mathbf{q}$, $\mathbf{i}$, and the EOS of (3).

To close the NHEC model we follow equations (58.11) and (58.12) of Landau and Lifshitz (1959) and adopt the parameterization

$$\mathbf{i} = -\rho_0 \kappa_s \nabla S, \qquad \mathbf{q} - (\mu - T\mu_\theta)\mathbf{i} = -\rho_0 C_{p0}\kappa_\theta \nabla\theta, \quad (10)$$

where C_{p0} is a constant equal to $4000\,\mathrm{J\,kg^{-1}\,^\circ C^{-1}}$ and κ_s and κ_θ are the kinematic diffusivities of salt and heat, respectively. Equation (10) acts to parameterize the unresolved grid-scale turbulent diffusion that tends to bring the fluid closer to an isohaline and isentropic state.

Only part of H (PE), called dynamic enthalpy H^D, contributes to the dynamics; the remaining part of H, called potential enthalpy H^P, represents the heat content of the system (Young 2010; McDougall 2003). In analogy to θ, H^P is simply the system's enthalpy when all parcels are displaced adiabatically to the reference pressure. H^P and

H^D are defined as

$$H = H^P + H^D, \quad H^P = \frac{\iint h^P \rho_0 \, \mathrm{d}y\mathrm{d}z}{\iint \rho_0 \mathrm{d}y\mathrm{d}z}, \quad H^D = \frac{\iint h^D \rho_0 \, \mathrm{d}y\mathrm{d}z}{\iint \rho_0 \mathrm{d}y\mathrm{d}z},$$
$$(11a)$$

$$h^P(\theta, S) = h(\theta, S, P_r), \qquad (11b)$$

$$h^D(\theta, S, P) = h(\theta, S, P) - h^P(\theta, S) = \int_{P_r}^{P} \left.\frac{\partial h}{\partial P'}\right|_{\theta,S} dP' = \int_{P_r}^{P} \frac{dP'}{\rho(\theta, S,}$$
$$(11c)$$

$$= (P - P_r)/\rho_0 + \int_z^0 b(\theta, S, z')\mathrm{d}z'. \qquad (11d)$$

Again P is the hydrostatic pressure by using Boussinesq approximation (Young 2010). The domain integral of $(P - P_r)/\rho_0$ in (11d) is approximately constant and does not contribute to the evolution of H^D (Young 2010). The

4

thermodynamic potentials of h^P and h^D are

$$C_p^P = \left.\frac{\partial h^P}{\partial \theta}\right|_S, \qquad C_p^D = \left.\frac{\partial h^D}{\partial \theta}\right|_{S,z} = \int_z^0 \left.\frac{\partial b}{\partial \theta}\right|_{S,z'} \mathrm{d}z', \tag{12a}$$

$$\mu^P = \left.\frac{\partial h^P}{\partial S}\right|_\theta, \qquad \mu^D = \left.\frac{\partial h^D}{\partial S}\right|_{\theta,z} = \int_z^0 \left.\frac{\partial b}{\partial S}\right|_{\theta,z'} \mathrm{d}z', \tag{12b}$$

$$C_p^P + C_p^D = C_p = \frac{T}{\theta}C_p^P, \qquad \mu^P + \mu^D = \mu - T\mu_\theta. \tag{12c}$$

Equation (12c) follows from (5b) and (8), and uses $T\partial\eta/\partial\theta|_S = (T/\theta)C_p^P$ (McDougall 2003).

By definition H^P can only be modified diabatically. By contrast, H^D relies on the vertical distribution of fluid and represents the gravitational PE (GPE), which is required to generate KE (see (14b) below). Similar to the derivation of (9), we evaluate $\partial h^D/\partial t$ and $\partial h^P/\partial t$ in terms of $\partial\theta/\partial t$ and $\partial S/\partial t$ (through thermodynamic potentials) and derive

$$\frac{\partial H^D}{\partial t} + \frac{\partial H^P}{\partial t} = -\frac{\partial \mathrm{KE}}{\partial t}, \tag{13a}$$

$$\frac{\partial H^D}{\partial t} = \frac{1}{\iint \rho_0 \mathrm{d}y\mathrm{d}z}\iint \frac{\partial h^D}{\partial t}\rho_0 \mathrm{d}y\mathrm{d}z = -\frac{\partial \mathrm{KE_{cum}}}{\partial t} - \frac{\partial \mathrm{C_{H^D toH^P}}}{\partial t} \tag{13b}$$

$$\frac{\partial H^P}{\partial t} = \frac{1}{\iint \rho_0 \mathrm{d}y\mathrm{d}z}\iint \frac{\partial h^P}{\partial t}\rho_0 \mathrm{d}y\mathrm{d}z = \frac{\partial \mathrm{Heat_{vis}}}{\partial t} + \frac{\partial \mathrm{C_{H^D toH^P}}}{\partial t}, \tag{14a}$$

$$\mathrm{KE_{cum}} = \mathrm{KE} + \mathrm{Heat_{vis}} = \frac{1}{\iint \rho_0 \mathrm{d}y\mathrm{d}z}\int_0^t \iint (wb)\,\rho_0 \mathrm{d}y\mathrm{d}z\,\mathrm{d}t, \tag{14b}$$

$$\mathrm{Heat_{vis}} = \frac{1}{\iint \rho_0 \mathrm{d}y\mathrm{d}z}\int_0^t \iint \nu(\nabla^2\psi)^2 \rho_0 \mathrm{d}y\mathrm{d}z\,\mathrm{d}t, \tag{15a}$$

$$\mathrm{C_{H^D toH^P}} = -\frac{1}{\iint \rho_0 \mathrm{d}y\mathrm{d}z}\int_0^t \iint \left[\frac{C_p^D \nabla\cdot(C_{p0}\kappa_\theta\nabla\theta)}{C_p} + \frac{C_p^D\nu(\nabla^2\psi)^2}{C_p}\right.$$
$$\left. + \mu^D\nabla\cdot(\kappa_s\nabla S) + \frac{C_p^D\kappa_s\nabla S\cdot\nabla(\mu^P+\mu^D)}{C_p}\right]\rho_0\mathrm{d}y\mathrm{d}z\,\mathrm{d}t. \tag{15b}$$

$\mathrm{Heat_{vis}}$ is the cumulative viscous dissipation of KE (Figure 1). $\mathrm{KE_{cum}}$ is the cumulative KE production by vertical buoyancy flux (derived from $\psi\times$ (2)). $\mathrm{C_{H^D toH^P}}$ is the time-integral of the rate of energy conversion of H^D to H^P (expressed using (10)), which depends on the unpredictable turbulent diabatic processes and can not be determined *a priori* (section 4c).

In contrast to H^P, H^D contributes little to the system's heat content, because

$$\frac{\partial h^D/\partial\theta}{\partial h^P/\partial\theta} = \frac{C_p^D}{C_p^P} = \frac{T-\theta}{\theta} < 0.3\%, \tag{16}$$

following (12a) and (12c). Thus the H^D variation is insensitive to the nonconservation of θ.

b. Numerical scheme

Equations (2), (3), (4a), (6), (10) define a closed system for numerical integration. Throughout this paper, except section 3, we use the full nonlinear EOS (Jackett et al. 2006). We compute h^P, h^D and their derivatives (μ^P, C_p^P, μ^D and C_p^D) using the state functions of Jackett et al. (2006). We use periodic boundaries in y and stress-free, zero-flux boundaries at the top/bottom. We discretize Laplacians using second-order-centered finite differences. We compute Jacobians following Arakawa (1997). We use the Adams-Bashforth scheme (Press 2007) for time integration. To resolve cabbeling instability, our default grid resolution is 0.83 m × 0.83 m. To ensure numerical stability while minimally affecting the turbulence, our default vertical and horizontal viscosity and tracer diffusivity are $3\times10^{-4}\,\mathrm{m^2/s}$. This model conserves salinity to within the round-off error of the computer, and conserves energy to within 5% of the KE (PE+KE deviates by <5% of KE) in almost all simulations.

3. KE contributions from OCAPE and the reduction of stratification

In this section we temporarily exclude cabbeling to isolate and explain the contributions of $\mathrm{S_{tb}}$ (section 3a–3b) and $-\mathrm{S_{strat}}$ (section 3c). This also helps to illustrate the effects of cabbeling when it is included later (section 4a). We use the following EOS for (3) that includes thermobaricity but excludes cabbeling (see Equation (29) of Ingersoll 2005),

$$b(\theta, S, z) = -g(\rho - \rho_0)/\rho = [\alpha_\theta(z)\delta\theta - \beta(z)\delta S]\,g. \tag{17}$$

Here $\delta\theta$, δS are departures of θ and S, respectively, from the basic state (θ_0, S_0). This basic state is the mean of the CFW and the WSW in the initial profile. The thermal expansion coefficient (α_θ) and the saline contraction coefficient (β) are functions of pressure with respect to θ_0 and S_0, and are computed from the full EOS (Jackett et al. 2006).

a. Unstratified simulation without cabbeling

We start with the a simple case: excluding cabbeling by using (17), and excluding stratification by employing an idealized initial two-layer unstratified profile: a CFW layer (0–0.5 km, -1.6 °C, 34.47 psu) overlying a WSW layer
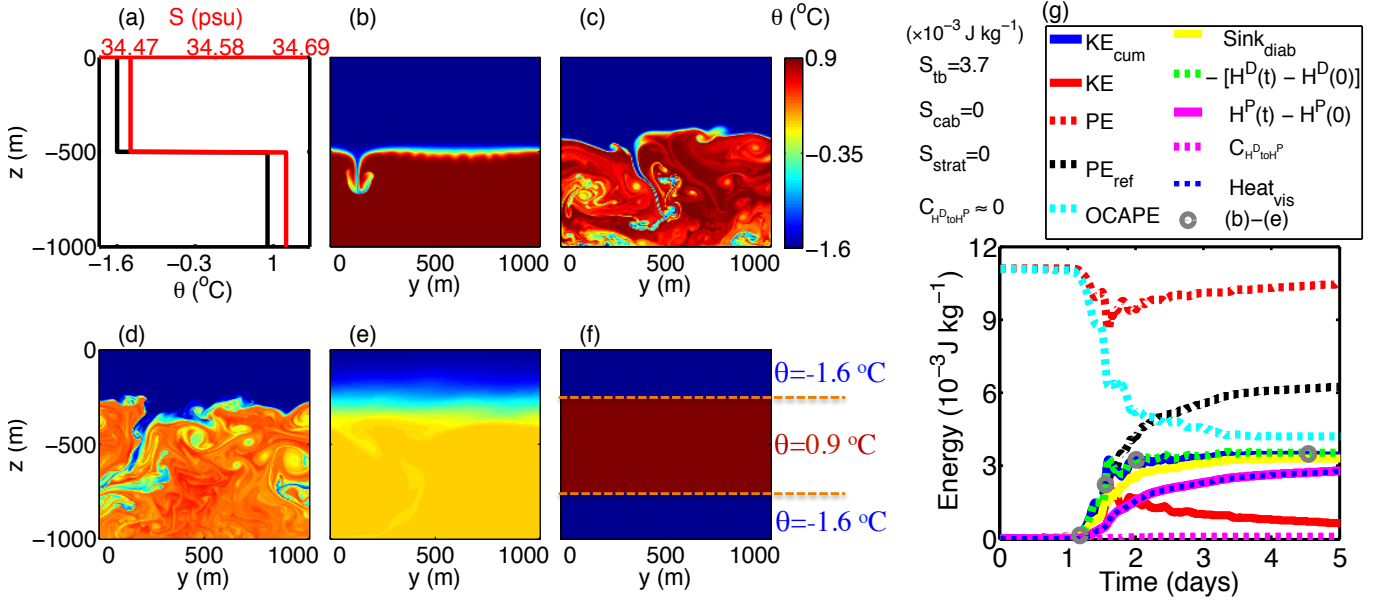
FIG. 2. Unstratified simulation without cabbeling in the EOS, as discussed in section 3a. z and y are the vertical and horizontal coordinates, respectively. (a) The initial θ/S profile. Snapshots of the θ (°C) field are shown (b) at t=1.18 days, (c) at t=1.56 days, (d) at t=2.01 days, and (e) at t=4.54 days (the quasi-steady state after convection). (f) The reference (minimum PE) state for the initial profile. (g) Time series of the energy budget (curves). We also show values of the four KE contributions (S_{tb}, S_{cab}, $-S_{strat}$ and $-C_{H^D toH^P}$) based on the whole convection (Equation (1)). See Figure 1 for the detailed energy relations. S_{cab}, S_{strat} and $C_{H^D toH^P}$ are all about zero here since the simulation excludes cabbeling and has a zero initial stratification ($C_{H^D toH^P}$ also relies on cabbeling, see section 4c). OCAPE is equal to PE minus PE_{ref} (the PE of the reference state). Both PE and PE_{ref} are computed relative to the initial PE_{ref}. The sinks of OCAPE include S_{tb} and $Sink_{diab}$: S_{tb} is the cumulative contribution of OCAPE to KE (Figure 1), while $Sink_{diab}$ is the cumulative dissipation of OCAPE by diabatic processes (defined in (18b)).

(0.5–1 km, 0.9 °C, 34.67 psu) (Figure 2(a)). From Part I we analytically determine its reference (minimum PE) state (Figure 2(f)). The column-averaged OCAPE is 1.1×10^{-2} J/kg. In this configuration the release of OCAPE can be triggered by infinitesimal vertical perturbations of the CFW into the WSW. Our domain size is $L \times L$ where L equals 1 km. To trigger the release of OCAPE we impose a uniform surface cooling of 100 W m^{-2} for 0.1 days between $y = L/12$ and $L/6$. The KE produced by this cooling is negligible. Ekman pumping caused by wind forcing could also trigger the convection (*e.g.*, Weiss et al. 1991; Schmid et al. 2008).

Figure 2(b)–(e) shows a series of simulated convection snapshots. The imposed surface cooling induces small velocities at the CFW/WSW interface and perturbs the initial plume of CFW into the WSW (Figure 2(b)). The plume gains negative buoyancy by thermobaricity as it descends. The velocity shear at the margins of the plume induces secondary Kelvin-Helmholtz instabilities. This generates local turbulent stirrings at smaller and smaller length scales. Our 2D system does not conserve vortic-

ity and thus does not develop an inverse cascade of energy. The turbulence perturbs the CFW/WSW interface and induces a succession of descending CFW plumes that convert OCAPE into KE. Thus convection becomes a self-sustaining process and the interface rises accordingly until the new interface is no longer unstable to turbulent perturbations. The convective motions are largely dissipated by $t = 2.3$ days (Figure 2(e)).

Figure 2(g) shows the time evolution of energy diagnostics. According to (13b)–(14a), H^D (dashed green curve) is converted to KE (solid red curve) via KE_{cum} (solid blue curve), and to H^P (solid magenta curve) via $C_{H^D toH^P}$ (dashed magenta curve). H^P also gains energy from viscous dissipation (Heat$_{vis}$, dashed blue curve) (Figure 1). Here $C_{H^D toH^P}$ is negligible due to the absence of cabbeling (section 4c). S_{cab} and S_{strat} are zero due to the absence of cabbeling and initial stratification. Therefore, according to (1), the only contribution to KE_{cum} is S_{tb} due to thermobaricity (OCAPE). OCAPE is defined as the PE minus the reference-state PE (PE_{ref}). As our isolated system conserves (KE+PE) and has no KE initially, it follows

that $PE(0) = PE(t) + KE(t)$. Thus the cumulative loss of OCAPE is

$$OCAPE(0) - OCAPE(t) = KE(t) + PE_{ref}(t) - PE_{ref}(0) = KE_c$$
$$(18a)$$

$$Sink_{diab}(t) = [PE_{ref}(t) - PE_{ref}(0)] - Heat_{vis}(t).$$ (18b)

Therefore, OCAPE has two sinks: KE_{cum} (equal to S_{tb} for this scenario) and $Sink_{diab}$. Here $Sink_{diab}$ is due to diabatic modification of the reference state (since PE_{ref} is constant for adiabatic processes; see Part I), and the viscous heating ($Heat_{vis}$).

As shown in Figure 2(g), for the initial OCAPE, $\sim 31.9\%$ is released to KE_{cum} and $\sim 31.1\%$ is removed diabatically via $Sink_{diab}$ (solid yellow curve), leaving $\sim 34.7\%$ unreleased. This $\sim 1/3$ conversion ratio of OCAPE to KE_{cum} is essentially independent of the initial trigger (as long as its direct contribution to KE is small). This ratio is also insensitive to the viscosity/grid resolution (Table 1): As viscosity tends to zero, the dissipation scale becomes smaller such that the energy dissipation equals the cascade rate of turbulent energy (*e.g.*, Vallis 2006).

b. Contribution of thermobaricity (OCAPE) to KE: S_{tb}

We demonstrate that S_{tb} is $\sim 1/3$ of OCAPE for any two-layer unstratified profile. For stratified profiles, a similar $1/3$ ratio still holds (section 3c; (21b)-(21c)). This ratio holds in the presence of cabbeling since thermobaricity and cabbeling contribute independently to KE_{cum} (section 1). Table 2 details four simulations without cabbeling (cases 2.1-2.4): their profiles are all initially unstratified and two-layer, with the CFW/WSW interface lying at different depths. In all simulations, $\sim 1/3$ of the initial OCAPE is consistently converted to KE_{cum} (*i.e.* S_{tb} here). Further, $C_{H^D toH^P}$ is negligible (see section 4c).

We now derive the $1/3$ OCAPE-to-KE_{cum} conversion ratio analytically. Only the H^D part of PE contributes to OCAPE (since H^P is constant for adiabatic processes). Further, $C_{H^D toH^P}$ is negligible in the absence of cabbeling. From (13b) we derive

$$\frac{KE_{cum}}{OCAPE} = \frac{H_i^D - H_f^D - C_{H^D toH^P}}{PE_i - PE_{ref}} \approx \frac{H_i^D - H_f^D}{H_i^D - H_{ref}^D}. \quad (19)$$

Here the subscripts i, f and ref denote the initial, the final, and the initial reference states. The initial reference state is determined following Part I. $(H_i^D - H_{ref}^D)$ is expressed following (11a), (11d) and (17). $(H_i^D - H_f^D)$ is expressed by (A10), with an unknown D_f (the depth of the upper boundary of CFW/WSW mixture in the final state; Figure 3(c)). Here we determine the value of D_f that maximizes[2] $(H_i^D - H_f^D)$, which predicts a D_f that is in agreement with the simulations mentioned above. This

---

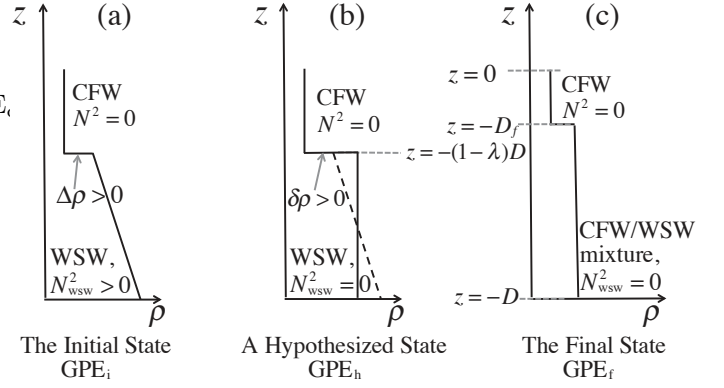[2] In (A10), $\gamma_{\theta\theta}$, N_{WSW}^2 and $\delta\rho$ are zero since we exclude cabbel-

FIG. 3. Schematic of three states for illustrating the reduction of stratification (N^2) during convection, which leads to a KE sink: $-S_{strat}$, as discussed in section 3c. (a) The initial state. It has a stable density jump $\Delta\rho$ at the CFW/WSW interface and a stratified WSW ($N^2 = N_{WSW}^2$). ρ is the density variation associated with N^2: $\rho = \int_{-D}^{z}(-\rho_0/g)N^2(z)dz$. (b) A hypothesized state, same as the initial state except taking the mean property of WSW from the initial state (*i.e.* from the dash to the solid line). $\delta\rho$ is the change of ρ from the bottom of CFW to the middle depth of WSW, defined in (20b) (states in (a) and (b) have the same $\delta\rho$). (c) The final quasi-steady state after convection, with a interface at depth $z = -D_f$. The gravitational potential energy (GPE) of these three states are GPE_i, GPE_h and GPE_f, respectively. Then $-S_{strat}$ is equal to $(GPE_i - GPE_h) + (GPE_h - GPE_f)$.

.

strategy of solving the final state (D_f) is consistent with the principle that a system tends to deform to a final state that minimizes PE (*i.e.* H_f^D here) (Reddy 2002). Using a linearly depth-dependent α_θ profile and a constant β, the predicted $KE_{cum}/OCAPE$ by (19) is exactly $1/3$ (with deviation $\leq 6\%$ if using realistic α_θ and β profiles). This $1/3$ ratio reveals the fundamental relation between the PE released by adiabatic movement of CFW (OCAPE) vs. the PE released by mixing of CFW into WSW (KE_{cum}).

c. Contribution of reduced stratification to KE: $-S_{strat}$

Conceptually, mixing out the stratification of an ocean column during convection raises the water column's center of mass. This would convert KE to GPE by an amount S_{strat} as quantified below. We again exclude cabbeling. We only modify our previous two-layer initial profiles by adding the stratification: a stable density gap $\Delta\rho$ across the CFW/WSW interface and a uniform positive stratifi-

---

ing and stratification here. D is a constant. Thus we determine D_f that maximizes $(H_i^D - H_f^D)$ by solving $d(A10)/dD_f = 0$ and $d^2(A10)/dD_f^2 < 0$. In this scenario, the analytical expression for D_f is zero when $\lambda > 2/3$ and is $(1 - 3/2 \times \lambda)D$ when $\lambda \leq 2/3$.

KE_{cum} \ dz	No cabbeling, in §3a				Full EOS, in §4a				Full EOS, case 4.4 in §4d			
ν	1.67m	1.11m	0.83m	0.67m	1.67m	1.11m	0.83m	0.67m	1.67m	1.11m	0.83m	0.67m
3×10^{-4}m^2/s	x	x	30.1%	31.5%	x	x	64.6%	64.7%	x	x	89.7%	90.2%
1×10^{-3}m^2/s	33.6%	32.4%	31.8%	31.6%	65.6%	68.2%	67.2%	65.0%	94.5%	91.0%	89.5%	90.5%
3×10^{-3}m^2/s	32.1%	32.6%	31.4%	34.5%	67.4%	66.4%	66.8%	69.0%	92.8%	94.1%	94.4%	89.7%

TABLE 1. Sensitivity of KE_{cum}, as a fraction of the initial OCAPE, to viscosity ν (same value as diffusivity) and grid resolution (dz=dy). The first reference simulation (in §3a) has thermobaricity but no cabbeling and stratification, with initial OCAPE=1.1×10^{-2} J/kg; The second (in §4a) has thermobaricity and cabbeling but no stratification, with initial OCAPE=1.1×10^{-2} J/kg; The third (case 4.4 in §4d) has all three effects, with initial OCAPE=3.9×10^{-3} J/kg. Their model domain dimensions are 1000 m $\times$ 1000 m, 1000 m $\times$ 1000 m and 700 m $\times$ 700 m, respectively. In all simulations except the ones denoted as "x", the flow is resolved without unphysical KE accumulation at the grid scale. The results indicate that KE_{cum} are insensitive (variation $< 5\%$) to ν and dz (as long as they are small enough to enable cabbeling instability if cabbeling is allowed; see section 6.1 of Harcourt 2005).

cation in the WSW layer ($N^2 = N^2_{WSW}$=constant). We consider scenarios in which the initial WSW is stratified in salinity only.

Figure 3 shows schematics of the initial and the final states of convection: D is the water column's depth and λ is the initial fraction of WSW of the whole column. We also consider a hypothesized state (Figure 3(b)), the same as the initial state except that the stratified WSW is replaced by the mean WSW. The GPEs of these three states (Figure 3(a)–(c)) are denoted as GPE$_i$, GPE$_h$, and GPE$_f$, respectively. Excluding thermobaricity and cabbeling, we derive (GPE$_i$ − GPE$_h$) and (GPE$_h$ − GPE$_f$) by multiplying gravity g by the change of depth of the water column's center of mass in either case. They are expressed by the first and the second brace term in (20a) below, respectively. Their sum is (GPE$_i$ − GPE$_f$) due to the reduction of stratification, *i.e.*, equal to

$$-S_{strat} = \left\{ -\frac{1}{12}N^2_{WSW}\lambda^3 D^2 \right\} + \left\{ -\frac{1}{2}\lambda\left[(1-\lambda)D - D_f\right]\frac{\delta\rho}{\rho_0}g \right\} \tag{20a}$$

$$\delta\rho = \Delta\rho + \frac{\rho_0 N^2_{WSW}\lambda D}{2g}. \tag{20b}$$

Equation (20a) is consistent with a more rigorous derivation from Appendix A ((A10)-(A11)).

Therefore, in the absence of cabbeling, we derive KE_{cum} following (A1) and (A10):

$$KE_{cum} = H^D_i - H^D_f = S_{tb} - S_{strat}, \tag{21a}$$

$$S_{tb} = \frac{1}{3}OCAPE_c(\delta\rho = 0) \tag{21b}$$

$$= \frac{1}{3}\left\{ -g\alpha_z\Delta\theta D^2\left[\lambda(\lambda-1)(1-2\lambda) + (2\lambda-3\lambda^2)\frac{D_f}{D} - \lambda\frac{D_f^2}{D^2}(1)\right]\right\} \tag{21c}$$

Denotations follow Appendix A. Here OCAPE$_c$ is the initial-state OCAPE for the part of water column where

convection occurs[3]. For unstratified profiles, this solution simply reduces to $S_{tb} = (1/3)$OCAPE, as in section 3b. Following section 3b, we predict the final state *a priori* by determining a D_f that maximizes $(H^D_i - H^D_f)$. At any instant during convection, the associated state cannot be determined *a priori* from initial conditions, and thus S_{tb} and S_{strat} (and also S_{cab}) at that instant cannot be determined analytically. In table 3, we detail eight numerical test simulations with different stratifications. In all cases KE_{cum} and D_f are well predicted by (21a) and the strategy above, respectively.

4. KE contributions from cabbeling-induced volume reduction and the conversion of H^D to H^P

In this section, we illustrate that cabbeling alone induces two KE components: S_{cab} and $-C_{H^D toH^P}$. Harcourt (2005) notes that the CFW/WSW transition is of finite vertical extent due to mixed layer entrainment or shear, which is key to inducing the cabbeling instability. Harcourt (2005) discussed the model capabilities needed to resolve cabbeling instability (see section 6.1 there). Following these requirements, our simulation adopts the full nonlinear EOS (Jackett et al. 2006) and prescribes a initial CFW/WSW interface of finite thickness ($\sim$20 m; section 4d), with numerical grid sizes of 0.83 m and a viscosity of 3×10^{-4}m^2/s.

a. Unstratified simulation with cabbeling

We reproduce the same simulation in section 3a (Figure 2) but now using the full EOS (Figure 4). This comparison identifies significant differences introduced by cabbeling: The initialization of convection is more rapid ($\sim$0.22

[3]Since convection only occurs from $z = -D_f$ to $-D$, when expressing OCAPE$_c$ using the OCAPE equation ((17c) of Part I), we should replace D, λ and $\Delta\rho$ by $(D - D_f)$, $\lambda D/(D - D_f)$ and $\delta\rho$, respectively, and finally multiply by a factor $(D - D_f)/D$. This gives (21c), as consistent with (A10) and (A11).

	Case 2.1	Case 2.2	Case 2.3	Case 2.4
Interface depth of initial state (CFW above WSW)	100 m	300 m	500 m	700 m
Initial reference state (by depths)	WSW, 0-900 m CFW, 900-1000 m	WSW, 0-700 m CFW, 700-1000 m	CFW, 0-250 m WSW, 250-750 m CFW, 750-1000 m	CFW, 0-550 m WSW, 550-850 m CFW, 850-1000 m
Depth of the upper boundary of CFW/WSW mixture at the final quasi-steady state	$\sim$ 0 m	$\sim$ 0 m	$\sim$ 250 m	$\sim$ 550 m
Initial OCAPE	2.7×10^{-2} J/kg	3.1×10^{-2} J/kg	1.1×10^{-2} J/kg	2.0×10^{-3} J/kg
KE_{cum} (% of initial OCAPE)	32.9%	34.5%	31.9%	31.1%
$Sink_{diab}$ (% of initial OCAPE)	66.9%	64.1%	31.1%	24.9%
Remaining OCAPE (% of initial OCAPE)	0.5%	0.8%	34.7%	43.0%
$C_{H^D toH^P}$ (% of initial OCAPE)	0.15%	0.06%	0.04%	0.11%

TABLE 2. Characterization of unstratified simulations without cabbeling in the EOS, as discussed in section 3b. We show the initial OCAPE, its two sinks: KE_{cum} and $Sink_{diab}$ (see (18a)), and the remaining OCAPE after convection. All simulations have a 1000 m × 1000 m modeling domain. They all have the CFW (θ=-1.6 °C, S=34.47 psu) overlying the WSW (θ=0.9 °C) initially but with different CFW/WSW interface depths. The S of the initial WSW is 34.63 psu, 34.65 psu, 34.67 psu, 34.69 psu, respectively, for Cases 2.1–2.4 to ensure a zero stratification ($N^2 = 0$). Their experimental configurations are otherwise identical to the reference simulation in Figure 2 (Case 2.3). About 1/3 of OCAPE is consistently released to KE_{cum} for all these simulations. $C_{H^D toH^P}$ is the energy conversion of dynamic enthalpy to potential enthalpy (see (15b)), which is consistently negligible for no-cabbeling simulation (see explanation in section 4c).
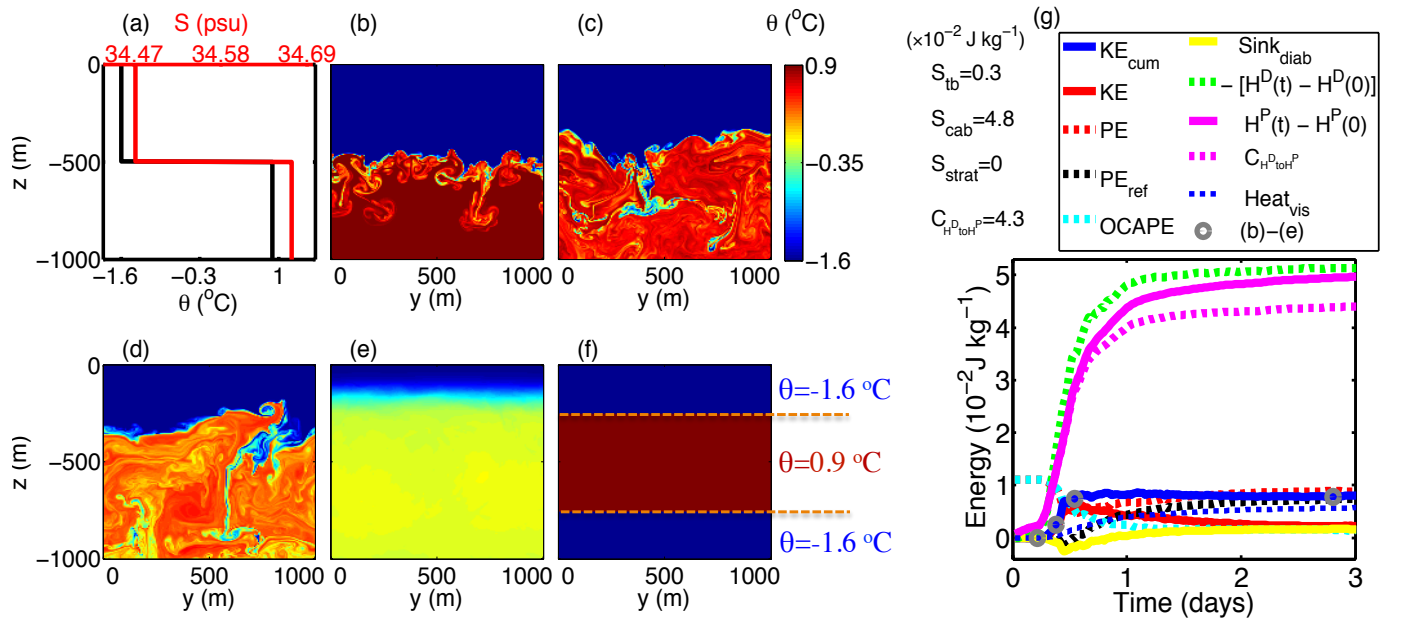
FIG. 4. As Figure 2 but for an unstratified simulation with cabbeling included in the EOS, discussed in section 4a. It is the same simulation as that in Figure 2 but uses the full nonlinear EOS of seawater (Jackett et al. 2006). Snapshots of the model's θ (°C) are shown (b) at t=0.22 day, (c) at t=0.38 day, (d) at t=0.53 day, and (e) at t=2.71 days. For (g), see Figure 1 for the detailed energy relations.

day vs 1.18 day) since cabbeling-involved entrainment/mixing at the initial interface generates neg-

ative buoyancy and entrains CFW plumes into WSW more rapidly (Harcourt 2005). Additional accelera-

	Case 3.1	Case 3.2	Case 3.3	Case 3.4	Case 3.5	Case 3.6	Case 3.7	Case 3.8
λ	0.9	0.9	0.9	0.9	0.7	0.7	0.7	0.7
$\Delta\rho$ (kg/m³)	0	8×10^{-3}	2×10^{-3}	4×10^{-3}	12×10^{-3}	0	1×10^{-3}	6×10^{-3}
N^2_{wsw} (s⁻²)	0.6×10^{-7}	0	0.2×10^{-7}	0.4×10^{-7}	0	1.0×10^{-7}	0.8×10^{-7}	0.4×10^{-7}
$\delta\rho$ (kg/m³)	2.8×10^{-3}	8.0×10^{-3}	3.0×10^{-3}	5.9×10^{-3}	12×10^{-3}	3.7×10^{-3}	3.9×10^{-3}	7.5×10^{-3}
OCAPE (J/kg)	2.39×10^{-2}	1.92×10^{-2}	2.37×10^{-2}	2.10×10^{-2}	0.89×10^{-2}	2.32×10^{-2}	2.30×10^{-2}	1.61×10^{-2}
$\mathrm{S_{tb}}$ (J/kg) by (21b)	8.8×10^{-3}	8.8×10^{-3}	8.8×10^{-3}	8.8×10^{-3}	5.8×10^{-3}	10.0×10^{-3}	9.9×10^{-3}	8.6×10^{-3}
$-\mathrm{S_{strat}}$ (J/kg) by (20a)	-4.9×10^{-3}	-3.4×10^{-3}	-2.5×10^{-3}	-5.0×10^{-3}	-4.7×10^{-3}	-6.3×10^{-3}	-5.9×10^{-3}	-6.3×10^{-3}
$\mathrm{KE_{cum}}$ (J/kg) by (21a)	3.9×10^{-3}	5.4×10^{-3}	6.3×10^{-3}	3.8×10^{-3}	1.1×10^{-3}	3.7×10^{-3}	4.0×10^{-3}	2.3×10^{-3}
$\mathrm{KE_{cum}}$ (J/kg) by simulation	4.1×10^{-3}	5.3×10^{-3}	6.5×10^{-3}	3.7×10^{-3}	1.2×10^{-3}	3.6×10^{-3}	4.3×10^{-3}	2.6×10^{-3}
D_f (m) by theory	0	0	0	0	185	22	27	96
D_f (m) by simulation	0	0	0	0	~ 190	~ 30	~ 30	~ 110

TABLE 3. Characterization of stratified simulations without cabbeling in the EOS, as discussed in section 3c. All simulations have a 1000 m × 1000 m modeling domain. They all have the same configurations (*e.g.* the θ and S of the initial CFW, the θ of the initial WSW, and the initial cooling) as the reference simulation in Figure 2 except the following parameters: λ, $\Delta\rho$, N^2_{wsw} and $\delta\rho$ (see the text for their definitions). The S of the initial WSW in each case can be determined by $\Delta\rho$ and N^2_{wsw}. OCAPE also differs from one case to another. $\mathrm{S_{tb}}$ and $(-\mathrm{S_{strat}})$ are the KE contributions from thermobaricity and the reduction of stratification, respectively. D_f is the depth of the upper boundary of CFW/WSW mixture at the final state. "D_f by theory" maximizes $H_i^D - H_f^D$ as given by (21a) along with (21c) and (20a). In all simulations $\mathrm{KE_{cum}}$ and D_f are both well predicted by (21a) and the strategy above, respectively.

tion of plumes by cabbeling also shortens the whole convective period ($\sim$2.5 day vs 3.5 day; see Figures 4(f) and 2(f)).

(ii) The interface depth of the final state (D_f) is shallower in the presence of cabbeling (~ 130 m vs 250 m). This is because a transient state with interface at 250 m depth is still susceptible to cabbeling instability that drags more CFW downward. This modification to the final state also leads to a smaller $\mathrm{S_{tb}}$ (0.0029 vs 0.0037 J/kg) following (21c).

(iii) Cabbeling contributes $\sim$0.005 J/kg to the final $\mathrm{KE_{cum}}$ by producing two additional terms: $\mathrm{S_{cab}} =$0.0481 J/kg and $-\mathrm{C_{H^D to H^P}} = -0.0432$ J/kg. The resulting $\mathrm{KE_{cum}}$ is more than doubled. $\mathrm{KE_{cum}}$ is insensitive to grid resolution and viscosity (Table 1). Therefore, in the presence of cabbeling, the energy budget should be updated from (21a) to

$$H_i^D - H_f^D = \mathrm{S_{tb}} - \mathrm{S_{strat}} + \mathrm{S_{cab}}, \qquad (22)$$

and Equation (1). These two equations are derived mathematically in Appendix A and are verified numerically in section 4d (Figure 7(a)–7(b)).

b. KE contribution from cabbeling-induced volume reduction: $\mathrm{S_{cab}}$

Cabbeling shrinks the water column's volume when the initial CFW and WSW are mixed by convection. This acts to lower the water column's center of mass and thus releases GPE to KE by an amount $\mathrm{S_{cab}}$. Again we consider initial states (Figure 3(a)) with WSW stratified in salinity only. Using the second-order Taylor series of potential density, the initial CFW and WSW both have a cabbeling term of density (see Equation (10) of Harcourt 2005):

$$\rho_i^c = -\rho_0 \gamma_{\theta\theta}(\Delta\theta)^2, \quad \gamma_{\theta\theta}(\theta, P, S) = -\frac{1}{2\rho_0}\left.\frac{\partial^2\rho}{\partial\theta^2}\right|_{P,S}, \quad (23)$$

where $\Delta\theta$ is the departure of the initial WSW from basic state θ_0, the mean θ of the initial CFW and WSW. Here $\gamma_{\theta\theta}$ is the coefficient of cabbeling (Harcourt 2005). We neglect other cabbeling terms related to $\partial^2\rho/\partial\theta\partial S$ and $\partial^2\rho/\partial S^2$ since $\gamma_{\theta\theta}$ dominates over them (Harcourt 2005). For wintertime polar seawater at sea level (*e.g.*, 30 psu$< S <$40 psu and $-2\,^\circ$C $< \theta < 4\,^\circ$C), $\gamma_{\theta\theta}$ is roughly constant: $(6.5 \pm 0.6) \times 10^{-6}\,^\circ$C^{-2} (Figure 3(a) of Huang 2014). $\gamma_{\theta\theta}$ varies by $< 10\%$ from sea level pressure to 1500 m depth (IOC et al. 2010). Thus we approximate $\gamma_{\theta\theta} \equiv 6.5 \times 10^{-6}\,^\circ$C^{-2} throughout for simplicity.

The CFW/WSW mixture of the final state, which has a thickness of $(D - D_f)$, assumes complete mixing (Figure 3(c); see simulations in Figures 2(e), 4(e), 5(e) and 7(e)). In contrast to (23), this final CFW/WSW mixture has a cabbeling density term:

$$\rho_f^c = -\rho_0 \gamma_{\theta\theta}(\Delta\theta_f)^2, \quad \Delta\theta_f = \left[2\lambda\frac{D}{D - D_f} - 1\right]\Delta\theta, \quad (24)$$
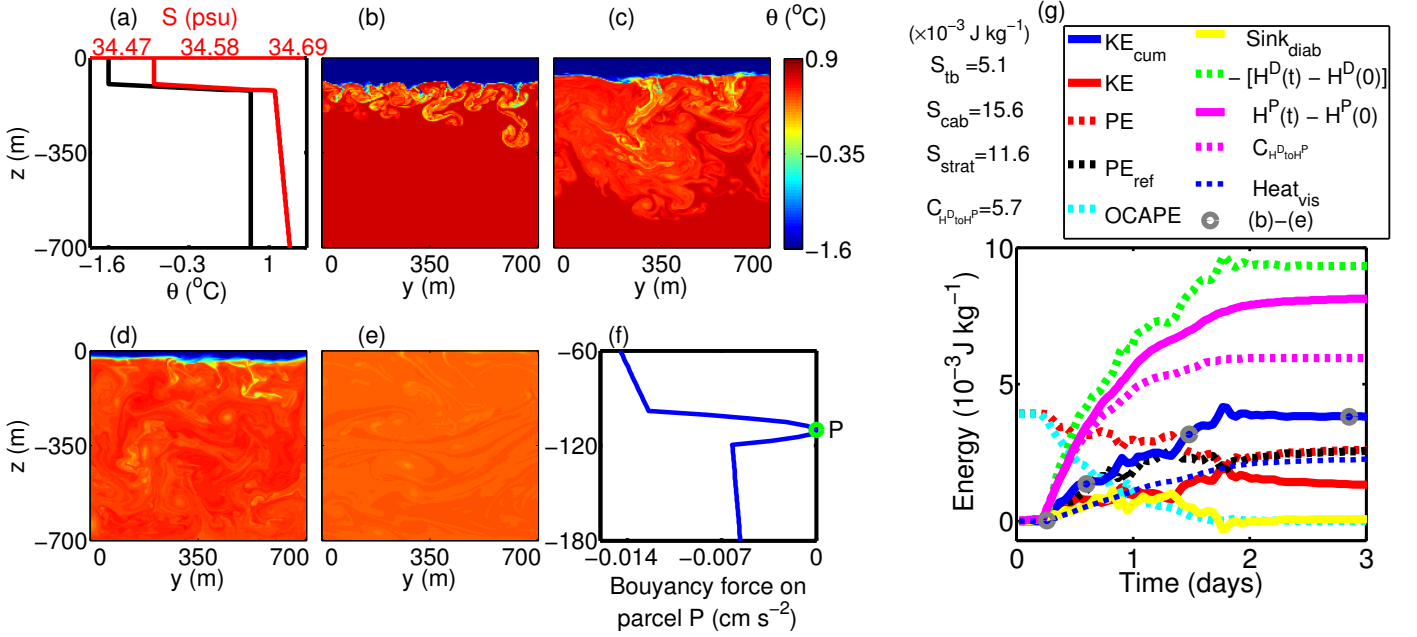
FIG. 5. As Figure 2, except panel (f), for a stratified simulation with cabbeling included in the EOS. This is case 4.4 of Table 4 discussed in section 4d. It adopts the full nonlinear EOS of seawater (Jackett et al. 2006) and a detailed model configuration is described in Table 4. Snapshots of the model's θ ($^{\circ}$C) are shown (b) at t=0.26 day, (c) at t=0.59 day, (d) at t=1.49 days, and (e) at t=2.8 days. Panel (f) follows Figure 9(b) of Harcourt (2005): it shows the buoyancy force on parcel P using the full nonlinear EOS when it is displaced vertically and adiabatically across the initial profile. Parcel P is originally located at the depth of 115 m within the initial interface (100-120 m depths). Panel (f) suggests a cabbeling instability when moving parcel P downward, since it becomes negatively buoyant. For (g), see Figure 1 for the detailed energy relations.

where $\Delta\theta_f$ is the CFW/WSW mixture's departure[4] from the basic state θ_0. Therefore, in a compressible fluid, cabbeling shrinks the CFW/WSW mixture's thickness by $(D-D_f)(\rho_f^c - \rho_i^c)/\rho_0$. Thus the center of mass of the whole column is lowered by $[(D-D_f)(\rho_f^c - \rho_i^c)/\rho_0](D+D_f)/(2D)$. Multiplying this by gravity g gives the release of GPE to KE by

$$
\begin{aligned}
S_{cab} &= \left[(D - D_f) \frac{\rho_f^c - \rho_i^c}{\rho_0} \frac{D + D_f}{2D} \right] \times g \\
&= 2g[\gamma_{\theta\theta}(\Delta\theta)^2](D + D_f)\left(\lambda - \lambda^2 \frac{D}{D - D_f} \right).
\end{aligned}
\tag{25}
$$

This expression agrees with a more rigorous derivation from Appendix A ((A10)-(A11)).

---

[4]For the expression of $\Delta\theta_f$ in (24), we neglect the nonconservation of θ during mixing because H^D (and thus S_{cab}) is insensitive to this nonconservation according to (16).

c. KE contribution from energy conversion of H^D to H^P: $-C_{H^D toH^P}$

$C_{H^D toH^P}$, as expressed in (15b), is the irreversible diabatic energy conversion of H^D to H^P, which reduces the KE production from H^D ((13b); Figure 1). We address the following question: why is $-C_{H^D toH^P}$ only significant in the presence of cabbeling (section 4a)?

We diagnose (15b) numerically and find that the first term dominates $C_{H^D toH^P}$:

$$
C_{H^D toH^P} \approx \frac{1}{\iint \rho_0 dydz} \int_0^t \iint -\frac{C_p^D \nabla \cdot (C_{p0}\kappa_\theta \nabla\theta)}{C_p} \rho_0 dydz \, dt,
\tag{26}
$$

Including cabbeling, the leading-order buoyancy expression is updated from (17) to be

$$
b(\theta, S, z) = \left[\alpha_\theta(z)\delta\theta - \beta(z)\delta S + \gamma_{\theta\theta}(\delta\theta)^2 \right] g.
\tag{27}
$$

11

Thus C_p^D, according to (12a), can be decomposed as follows:

$$C_p^D = \int_z^0 \left.\frac{\partial b}{\partial \theta}\right|_{S,z'} \mathrm{d}z' = C_p^\alpha + C_p^{cab}, \qquad (28a)$$

$$C_p^\alpha = \int_z^0 \alpha_\theta g \mathrm{d}z'; \quad C_p^{cab} = \int_z^0 2\gamma_{\theta\theta}\delta\theta g \mathrm{d}z' = (-z)2\gamma_{\theta\theta}\delta\theta g, \qquad (28b)$$

We diagnose numerically that the effect of C_p^{cab} dominates the factor C_p^D in (26), where C_p is approximately $C_{p0} = 4000\,\mathrm{J\,kg^{-1}\,^oC^{-1}}$. Thus we update (26) to

$$\mathrm{C_{H^D toH^P}} \approx \frac{1}{\iint \rho_0 \mathrm{d}y\mathrm{d}z} \int_0^t \iint -C_p^{cab}\nabla\cdot(\kappa_\theta\nabla\theta)\mathrm{d}y\mathrm{d}z\,\mathrm{d}t \qquad (29a)$$

$$= \frac{-2\gamma_{\theta\theta}g}{\iint \rho_0 \mathrm{d}y\mathrm{d}z} \int_0^t \iint \nabla(\delta\theta z)\cdot(\kappa_\theta\nabla\theta)\mathrm{d}y\mathrm{d}z\,\mathrm{d}t \qquad (29b)$$

$$\approx \frac{2\gamma_{\theta\theta}g}{\iint \rho_0 \mathrm{d}y\mathrm{d}z} \int_0^t \iint (-z)\kappa_\theta(\nabla\theta)^2\mathrm{d}y\mathrm{d}z\,\mathrm{d}t \quad > 0, \qquad (29c)$$

using (28b), the no-flux boundary condition and $\nabla(\delta\theta) = \nabla\theta$, and neglecting a small term proportional to $\partial(\delta\theta)^2/\partial z$. In (29c), $(-z)$ is always positive. Equation (29c) is verified numerically.

In summary, cabbeling contributes to heat capacity by a factor of $(\gamma_{\theta\theta}\delta\theta)$ as in (28b). This factor couples with the heat diffusion $\nabla\cdot(\kappa_\theta\nabla\theta)$ as in (29a) and generates a positive-definite contribution ($\propto (\nabla\theta)^2$) to $\mathrm{C_{H^D toH^P}}$ as in (29c), which accumulates over time. Thus $\mathrm{C_{H^D toH^P}}$ is only significant in the presence of cabbeling. From (29c), $\mathrm{C_{H^D toH^P}}$ is proportional to κ_θ as well as $(\nabla\theta)^2$, while the mean $(\nabla\theta)^2$ decreases with κ_θ. Thus these two factors act to compensate each other and induces the insensitivity of $\mathrm{C_{H^D toH^P}}$ to diffusivity κ_θ, as diagnosed numerically. Due to the process-dependent nature, $\mathrm{C_{H^D toH^P}}$, a component of $\mathrm{KE_{cum}}$ in (1), cannot be predicted *a priori*, but rather must be diagnosed numerically.

d. Stratified simulations with cabbeling

We conduct eight numerical experiments (Table 4). Since our energy decomposition (A10) relies on the ocean column depth D, we perform cases with various sizes of D to test the sensitivity. They initially all have a linear variation of θ and S across the CFW/WSW interface (100–120 m depths). But they have differing initial stratifications. The initial cooling applied to the simulation in Figure 2 is also applied to all simulations here, which triggers convection along with the cabbeling instability. For all simulations, $H_i - H_f$ and $\mathrm{KE_{cum}}$ are well predicted by (22) and (1) (Figure 6(a)–6(b)). As in Table 4, $\mathrm{S_{tb}}$ is larger than

$\mathrm{S_{cab}}$ for cases 4.7–4.8 (column depth= 2 km), while smaller than $\mathrm{S_{cab}}$ for cases 4.1–4.6 (column depth= 0.7 km). This is because $\mathrm{S_{tb}}$ and $\mathrm{S_{cab}}$ have a quadratic (see (21c)) and a near-linear (see (25)) dependence on column depth, respectively. We analyze case 4.4 in detail (Figure 5). The snapshots of convection resemble the simulation of Harcourt (2005) (see Figure 14(a) and 14(b) there). Following Harcourt (2005), Figure 5(f) suggests a cabbeling instability for the initial interface. Cabbeling contributes to the final $\mathrm{KE_{cum}}$ by $\mathrm{S_{cab}} - \mathrm{C_{H^D toH^P}} = 0.01$ J/kg, which is comparable to $\mathrm{S_{tb}} = 0.0051$ J/kg and $-\mathrm{S_{strat}} = -0.0116$ J/kg. $\mathrm{KE_{cum}}$ here is again insensitive to grid size and viscosity (Table 1).

e. A strategy to estimate the maximum depth of convection

Previous studies predict the maximum depth that convective plumes can reach using a Lagrangian approach: this approach follows an individual plume and estimates its acceleration based on entrainment assumptions (*e.g.*, Turner 1979; Akitomo 2007). Here we propose to estimate the maximum depth of convection from an energetic perspective by the followings steps.

(i) Begin with the initial θ and S profiles that have CFW overlying WSW with a column depth of D_{max}. We assume the final state of convection comprises a CFW layer on top for $-D_f \leq z \leq 0$, a CFW/WSW mixture at the middle for $-D \leq z \leq -D_f$, and a WSW layer below for $-D_{max} \leq z \leq -D$. Here D always denotes the maximum depth of convection, which also equals the ocean-column depth in previous sections.

(ii) The θ/S profile of the final state is a known function of the variables D_f and D: we assume that fluid in the regions $-D_f \leq z \leq 0$ and $-D_{max} \leq z \leq -D$ remain unmodified from the initial state. For $-D \leq z \leq -D_f$, θ and S are assumed to be homogeneous due to a complete mixing of the initial state within the corresponding depths (see, *e.g.*, Figures 2(e), 4(e) and 5(e))). Given the θ/S profiles above, the H^D difference between the initial and the final states, $(H_i^D - H_f^D)$, is given by (A10) in terms of D_f and D (or given by (11a) and (11d) using the full EOS).

(iii) We assume that the final state is the one that has the minimum PE, which is consistent with simulations (see below) and the principle of minimum total potential energy (Reddy 2002). While PE is defined as $H^D + H^P$ according to (7) and (11a), we use $\mathrm{PE} \approx H^D$ because H^P does not contribute to KE (see Figure 1). Here we only discuss the cases with $D_f = 0$ in the final state, which have realistic applications such as for Weddell Polynya (McPhee 2003; Harcourt 2005) (see also Figures 5(e) and 7(e)). Discussing nonzero D_f

12

	Case 4.1	Case 4.2	Case 4.3	Case 4.4	Case 4.5	Case 4.6	Case 4.7	Case 4.8
D (m)	700	700	700	700	700	700	2000	2000
$\Delta\rho$ (kg/m³)	1×10^{-3}	1×10^{-3}	5×10^{-3}	5×10^{-3}	9×10^{-3}	9×10^{-3}	5×10^{-3}	5×10^{-3}
N^2_{wsw} (s⁻²)	0.5×10^{-7}	2.5×10^{-7}	0.5×10^{-7}	2.5×10^{-7}	0.5×10^{-7}	2.5×10^{-7}	0.2×10^{-7}	0.8×10^{-7}
$\delta\rho$ (kg/m³)	2.6×10^{-3}	8.8×10^{-3}	6.6×10^{-3}	12.8×10^{-3}	10.6×10^{-3}	16.8×10^{-3}	7.0×10^{-3}	12.9×10^{-3}
OCAPE (J/kg)	1.33×10^{-2}	0.78×10^{-2}	0.98×10^{-2}	0.43×10^{-2}	0.62×10^{-2}	0.10×10^{-2}	5.77×10^{-2}	4.98×10^{-2}
S_{tb} (J/kg) by (21b)	5.1×10^{-3}	5.1×10^{-3}	5.1×10^{-3}	5.1×10^{-3}	5.1×10^{-3}	5.1×10^{-3}	20.9×10^{-3}	20.9×10^{-3}
$-S_{\mathrm{strat}}$ (J/kg) by (20a)	-2.3×10^{-3}	-1.0×10^{-2}	-4.1×10^{-3}	-1.16×10^{-2}	-5.6×10^{-3}	-1.33×10^{-2}	-8.9×10^{-3}	-2.87×10^{-2}
S_{cab} (J/kg) by (25)	15.6×10^{-3}	15.6×10^{-3}	15.6×10^{-3}	15.6×10^{-3}	15.6×10^{-3}	15.6×10^{-3}	17.5×10^{-3}	17.5×10^{-3}
$-C_{\mathrm{H^D toH^P}}$ (J/kg) by simulation	-7.0×10^{-3}	-6.2×10^{-3}	-7.4×10^{-3}	-5.6×10^{-3}	-6.6×10^{-3}	-4.6×10^{-3}	-4.5×10^{-3}	-4.1×10^{-3}

TABLE 4. Characterization of stratified simulations with cabbeling (using the full EOS), as discussed in section 4d. Denotations follow Table 3. In all simulations the horizontal size of the modeling domain is the same as its vertical size (*i.e.* D). All simulations initially have the same CFW (θ =-1.6°C, S=34.51 psu) at 0–100 m depths, a linear variation of θ and S across 100–120 m depths, and a WSW layer beneath (θ =0.7°C). The S of the initial WSW in each case can be determined by $\Delta\rho$ and N^2_{wsw}. The initial cooling applied to the simulation in Figure 2 is also applied to all simulations here. These perturbations, along with the cabbeling instability, trigger convection in the simulations. All simulations have a final state of total column mixing. See ($H_i - H_f$) and $\mathrm{KE}_{\mathrm{cum}}$ diagnosed from simulations here vs. the predictions by (22) and (1) in Figure 6(a)–6(b).

	Case 5.1	Case 5.2	Case 5.3	Case 5.4	Case 5.5	Case 5.6	Case 5.7	Case 5.8	Case 5.9
$\Delta\rho$ (kg/m³)	1×10^{-3}	1×10^{-3}	1×10^{-3}	5×10^{-3}	5×10^{-3}	5×10^{-3}	9×10^{-3}	9×10^{-3}	9×10^{-3}
N^2_{wsw} (s⁻²)	1×10^{-7}	2×10^{-7}	4×10^{-7}	1×10^{-7}	2×10^{-7}	4×10^{-7}	1×10^{-7}	2×10^{-7}	4×10^{-7}

TABLE 5. Characterization of stratified simulations with cabbeling (using the full EOS), focusing on the convection depth, as discussed in section 4e. Unlike Table 4, all simulations here do not have a convection depth that reaches the bottom of the 2000 m × 2000 m modeling domain. They all initially have a CFW (θ =-1.6°C, S=34.51 psu) at 0–100 m depths, a linear variation of θ and S across 100–120 m depths, and a WSW layer (θ =0.7°C) beneath. The S of the initial WSW in each case can be determined by $\Delta\rho$ and N^2_{wsw}. The initial cooling applied to the simulation in Figure 2 is also applied to all simulations here. All simulations have a final state where all CFW sinks into WSW (*i.e.* D_f=0). See the convection depths diagnosed from simulations here vs. our predictions in Figure 6(c).
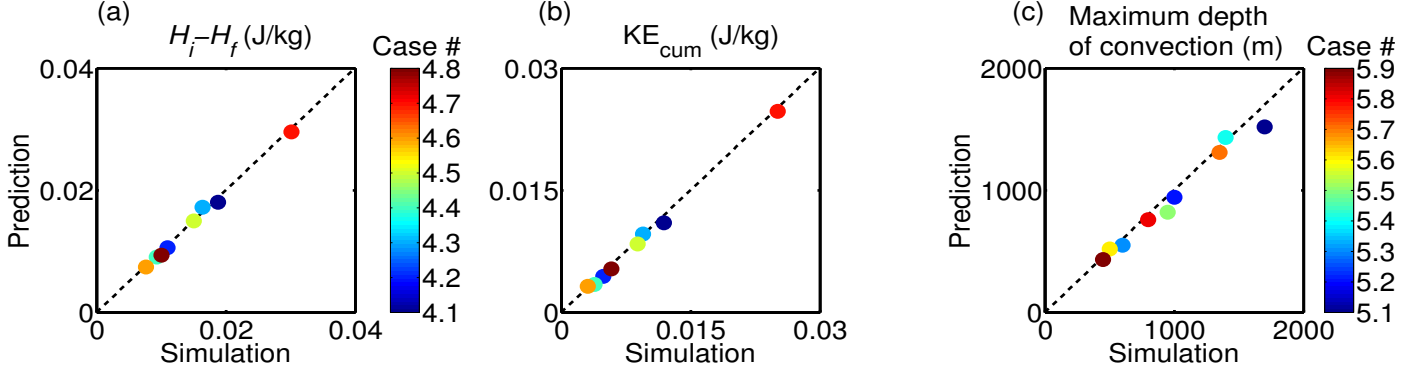

FIG. 6. (a) Prediction of $H_i - H_f$ by (22), (b) prediction of $\mathrm{KE}_{\mathrm{cum}}$ by (1) vs. numerical simulations for cases 4.1–4.8 described in Table 4. Here the prediction of $\mathrm{KE}_{\mathrm{cum}}$ adopts the value of $C_{\mathrm{H^D toH^P}}$ diagnosed from simulation since $C_{\mathrm{H^D toH^P}}$ has no analytical solution. Panels (a) and (b) share the same colorbar. (c) Prediction of the maximum depth of convection by our strategy in section 4e vs. numerical simulations for cases 5.1–5.9 described in Table 5. As shown in panels (a)-(c), these predictions agree closely with numerical simulations. All simulations here have a final state where all CFW sinks into WSW.
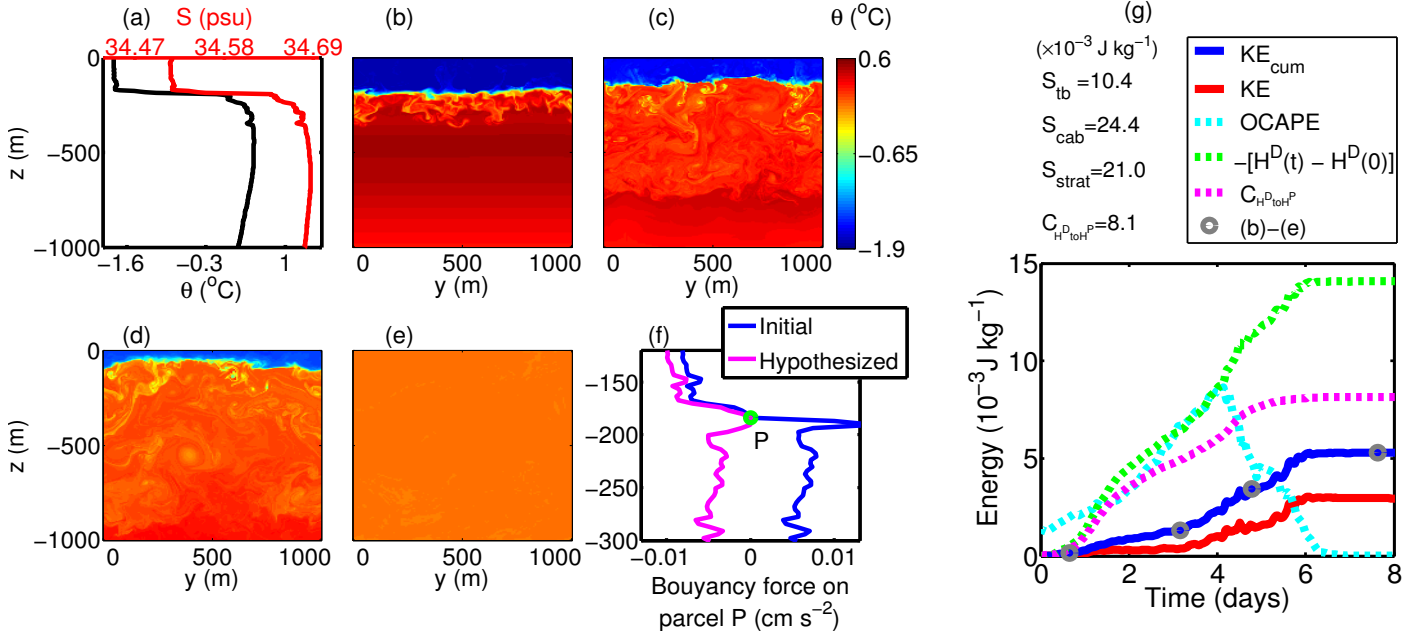
FIG. 7. As Figure 5 but for a stratified simulation with cabbeling based on realistic initial profiles, discussed in section 5. The model configuration is the same as that in Figure 5, except with a uniform surface salinity flux enforced from t=0 to t=4.2 days, equivalent to an ice formation rate of 1.5 cm/day. (a) The initial profile, from Maud Rise (65.4605°S, 2.4007°E) on August 2, 1994, station 48 of ANZFLUX CTD profile (courtesy of Bruce Huber; McPhee et al. 1996). 1000 m is about the maximum depth of convection in our simulation. Snapshots of the model's θ field are shown (b) at $t=0.65$ day, (c) at $t=3.1$ days, (d) at $t=4.7$ days, and (e) at $t=7.5$ days. Panel (f) is similar to Figure 5(f) but with a additional magenta curve computed from a hypothesized profile. It is the same as initial profile except with a saltier mixed layer (at 0–180 m depths) due to 6.3 cm of ice formation (*i.e.* 1.5 cm/day×4.2 days). It has a linear variation of θ and S across the CFW/WSW interface at 180–200 m depths. This magenta curve suggests that brine rejection may generate a cabbeling instability for parcel P at the interface (*i.e.* become negatively buoyant when it is moved downward). For (g), see Figure 1 for the detailed energy relations.

would also have important applications but is out of this manuscript's scope. Thus we determine the final state by solving for the value of D that maximizes[5] $(H_i^D - H_f^D)$. This solution for D is treated as the maximum depth of convection.

The assumption PE $\approx H^D$ above should be treated with caution: H^D is not converted completely to KE due to $C_{H^D \text{to} H^P}$, *i.e.* $\Delta H^D = \text{KE}_{\text{cum}} + C_{H^D \text{to} H^P}$ (Figure 1 and (13b)). Further, $C_{H^D \text{to} H^P}$ is process-dependent and cannot be determined *a priori* given the initial and the final

states (section 4c). The uncertainty by neglecting $C_{H^D \text{to} H^P}$ above in predicting the final state remains the focus of future studies. We test nine simulations with different initial stratifications (Table 5). Our predictions of the convection depth by the strategy above agree closely with those diagnosed from the numerical simulations (Figure 6(c)), which are diagnosed based on the maximum depth that convective plumes and the subsequent mixing can reach. This strategy may be useful in improving the parameterizations of deep convection in ocean models.

5. Application to observed profiles

We apply our analysis of energy and maximum depth of convection to an example with the initial profile (Figure 7(a)) obtained from the Weddell Sea. It has CFW over-

---

[5]We should maximize $(H_i^D - H_f^D)$ in units of J, as expressed by $((\text{A10}) \times D \times \rho_0 \times 1\text{m}^2)$ ((A10) has a unit of J/kg). In (A10), we use $D_f = 0$ and $\lambda = (1 - D_i/D)$ by definition (*i.e.*, λ varies with D), where D_i is the fixed initial depth of CFW. Thus we determine D by solving $\text{d}[(\text{A10}) \times D]/\text{d}D = 0$ and $\text{d}^2[(\text{A10}) \times D]/\text{d}D^2 < 0$.

14

lying WSW, with a interface at about 180–200 m depths. It has an OCAPE of 1.1×10^{-3} J/kg. Figure 7(f) (blue curve) suggests that the initial profile is not susceptible to cabbeling instability. To trigger convection in simulation, we impose a uniform surface salinity flux equivalent to an ice formation rate of 1.5 cm/day (e.g., Figures 11(c) of Harcourt 2005) since the initial mixed layer is at the freezing point. This idealized configuration ignores the ice-ocean dynamic interaction (e.g., see an associated parameterization in Harcourt 2005). The salinity flux is enforced for the first 4.2 days, which induces cabbeling instability at the interface (magenta curve in Figure 7(f)). Our simulation shows convective plumes continuously sinking from the interface (Figures 7(b)–7(d)), similar to the findings of Harcourt (2005). The surface flux introduces additional complications to the energetics (e.g., for H^P) and we focus on some key energy quantities (Figure 7(g)). H^D is still partitioned into KE_{cum} and $C_{H^D to H^P}$ ((13b) and Figure 1). OCAPE is generated and partially released simultaneously for the first 4.2 days due to the surface forcing. Evaluation of S_{tb} by (21b), S_{cab} by (25) and S_{strat} by (20a) give 0.0104, 0.0244 and 0.0210 J/kg, respectively, using the initial profile except with a saltier mixed layer by the 4.2 days' surface salt input[6]. $C_{H^D to H^P}$ is 0.0081 J/kg as diagnosed from simulation. These lead to $H_i^D - H_f^D = 0.0138$ J/kg by (22) and $KE_{cum}= 0.0057$ J/kg by (1); both agree with the simulation (Figure 7(g)). The strategy in section 4e predicts the maximum depth of convection $\sim$910 m, consistent with simulation ($\sim$1000 m in our test simulation, whose domain depth is 1500 m).

6. Discussion and Conclusion

a. Key results

We summarize our key results as follows:

(i) Dynamic enthalpy H^D is insensitive to the nonconservation of potential temperature (see (16)), allowing us to predict the change of H^D due to convection (Figure 6(a)).

(ii) The KE budget of Type II and Type III convection may be decomposed into four components (Equation (1) and Figure 1): (1) A source of KE due to thermobaricity/OCAPE; (2) A sink of KE due to the reduction of stratification by vertical mixing, which raises the water column's center of mass and converts KE to PE; (3) A source of KE due to cabbeling-induced shrinking of the water column's volume when water masses with different temperatures are mixed, which lowers the water column's center of mass and releases PE to KE; (4) A reduced production of KE due to

cabbeling-related diabatic energy conversion of dynamic enthalpy to potential enthalpy[7]. Our analysis is based on the initial profiles with CFW overlying WSW as widely observed in winter-time polar oceans. We assume that the initial WSW is stratified in salinity only. We derived analytical expressions to predict the first three components (Appendix A). The fourth component is diagnosed numerically (Table 4 and Figure 6(b)).

(iii) Thermobaricity (the first KE component above) dominates over cabbeling (the third KE component above) for deeper convection depths, while the latter dominates over the former for shallower convection depths (Table 4, cases 4.1–4.6 vs cases 4.7–4.8).

(iv) We develop a strategy to predict the maximum depth of convection from the initial profile, which is reproduced by the numerical simulations (Figure 6(c)).

b. Model limitations

Our simulations were designed to build up a conceptual understanding for the energy partitioning during convection. As a result, numerous physical processes that could affect convection have not been included. For example, abrupt vertical mixing during convection might couple with baroclinic instability (Akitomo 2005, 2006). Earth's rotation might impact the OCAPE/cabbeling dynamics directly via the Coriolis force (Harcourt 1999) and indirectly via the background geostrophic circulation/eddies. Double diffusive convection also occurs in two-layer stratifications (Radko et al. 2014) and may couple with thermobaric/cabbeling dynamics (e.g., Carmack et al. 2012). Other factors such as surface wind stress, topography and horizontal buoyancy gradient may also impact convection.

Our choice to use 2D simulations reduces the computational burden and permits a greater exploration of the parameter space. These 2D simulations fail to resolve 3D instabilities that may occur following deep convection and laterally mix the sinking water (Jones and Marshall 1997). However, the 2D and 3D associated simulations in Akitomo (2006) result in small differences. Our simulations use a constant viscosity, which may induce unrealistic effects (Harcourt 2005).

Type II and Type III convection may or may not be distinguished uniquely. It is difficult to distinguish them from the energetic perspective discussed in this study. It is possible that a more dynamical difference between these convection types may be identified from a buoyancy perspective (see Harcourt 2005) and should be investigated in a future study.

---

[6]Parameters are: $\Delta\theta \sim 1.115^oC$, $H = 1000$ m, $\lambda \sim 0.81$, $\delta\rho \sim 0.0101 kg/m^3$, $N^2_{wsw} \sim 3.06 \times 10^{-7} S^{-2}$.

[7]See Figure 1 (left) and section 2. There are only three energy reservoirs here: H^D, H^P and KE.

Our simulation includes viscous heating in the thermodynamic equation, which converts KE to PE. This is key for energy conservation (Landau and Lifshitz 1959) as well as for characterizing the dynamics (Figure 1). However, inclusion of viscous heating is not necessary for an accurate prediction of the convective dynamics. All viscous heating is converted to H^P (Figure 1), but only H^D contributes to the KE (Young 2010). Further, viscous heating causes negligible changes to the temperature field as well as to the buoyancy force, due to the large specific heat capacity of water. In this study we also account for the changes in thermodynamic potentials (*e.g.* chemical potential; see (12a)-(12c)). While these terms are not necessary for an accurate prediction of the convective evolution (recall that only (2), (3), (4a), (6), (10) define the closed model for numerical integration), they remain important for characterizing the dynamics.

The mixing parameterizations in current ocean general circulation models (GCMs) typically apply strong local diapycnal mixing in the vertical wherever the water column is statically unstable (*e.g.*, the KPP parameterization, Large et al. 1994). A parameterization for Type II and Type III convection, however, should include the vertical movement of ocean parcels to large depths without substantial mixing at intermediate depths. This paper may help improve this parameterization (*e.g.*, parameterize tracer diffusivities from the estimated KE and the convection depth). This may resemble the parameterizations of moist convection in atmospheric GCMs using CAPE (Gregory et al. 2000; Zhang 2009).

Appendix: Mathematical derivation of Equation (1)

Equation (1) summarizes our energy decomposition of the KE budget for Type II and Type III convection. In this appendix we derive (1) based on the whole convection. Following definitions and denotations in section 2a, from (13b) we derive

$$\text{KE}_{\text{cum}} = -\text{C}_{\text{H}^D\text{toH}^P} + (H_i^D - H_f^D), \qquad \text{(A1)}$$

where the subscripts 'i' and 'f' denote the initial and final states, respectively. Now we derive the expression of $(H_i^D - H_f^D)$ based on idealized initial/final states shown schematically in Figure 3. The initial state approximates widely observed quasi-two-layer stratification in wintertime polar oceans (Gordon and Huber 1990): it has a homogeneous CFW (constant θ_{CFW} and S_{WSW}) at depths $-(1-\lambda)D < z < 0$, overlying a constant-stratified WSW (θ_{WSW} and S_{WSW}, constant $N^2 = N^2_{\text{WSW}}$) at depths $-D < z < -(1-\lambda)D$ (Figure 3a). We only consider WSW stratified in salinity, *i.e.*, with θ_{WSW}=constant and S_{WSW} linear with depth:

$$\frac{\text{d}S_{\text{WSW}}(z)}{\text{d}z} = -\frac{N^2_{\text{WSW}}}{\beta g}, \qquad \text{(A2)}$$

following the definition of N^2 (Gill 1982). We use simplified Taylor series of buoyancy

$$b = g[(\alpha_0 + \alpha_z z)\delta\theta - \beta\delta S + \gamma_{\theta\theta}\delta\theta^2], \qquad \text{(A3)}$$

where α_0, α_z and β are treated constant following the denotations of Part I ($\alpha_z = -3 \times 10^{-8}\,^{\circ}\text{C}^{-1}\text{m}^{-1}$). $\gamma_{\theta\theta}$ is the constant cabbeling coefficient defined in section 4b. $\delta\theta$ and δS are the anomalies from the mean of the initial CFW and WSW properties

$$\delta\theta(z) = \theta(z) - 0.5(\theta_{\text{CFW}} + \theta_{\text{WSW}}), \qquad \delta S(z) = S(z) - 0.5(S_{\text{CFW}} + \text{)} \qquad \text{(A4)}$$

where $\overline{S_{\text{WSW}}}$ is the vertical mean of S_{WSW} in the WSW layer following (A2). We define

$$\Delta\theta = 0.5(\theta_{\text{WSW}} - \theta_{\text{CFW}}), \qquad \Delta S = 0.5(S_{\text{WSW}} - \overline{S_{\text{WSW}}}). \qquad \text{(A5)}$$

Then $\delta\rho$, the density difference between the CFW and the mean WSW at the level of the CFW/WSW interface initially, has an expression

$$\delta\rho = \rho_0\left[-(\alpha_0 - \alpha_z(1-\lambda)D) \times 2\Delta\theta - \beta \times 2\Delta S\right]. \qquad \text{(A6)}$$

Further, from (A4)-(A5) we get the vertical profiles of $\delta\theta$ and δS for the initial state

$$\begin{cases} \delta\theta_i = -\Delta\theta, \quad \delta S_i = -\Delta S, & \text{for} -(1-\lambda \\ \delta\theta_i = \Delta\theta, \quad \delta S_i = \Delta S - \dfrac{N^2_{\text{WSW}}}{\beta g}(z + (1-0.5\lambda)D), & \text{for} -D < z \end{cases} \qquad \text{(A7)}$$

where the upper and the lower describe the initial CFW and WSW, respectively. Similarly, we derive the final state: we assume that the CFW is unmodified for $-D_f < z < 0$ and the fluid column becomes completely mixed for $-D < z < -D_f$ (Figure 3c; based on numerical simulations such as Figures 2(e), 4(e) and 5(e)), *i.e.*,

$$\begin{cases} \delta\theta_f = -\Delta\theta, \quad \delta S_f = -\Delta S, & \text{for} - \\ \delta\theta_f = \dfrac{(2\lambda-1)D + D_f}{D - D_f}\Delta\theta, \quad \delta S_f = \dfrac{(2\lambda-1)D + D_f}{D - D_f}\Delta S, & \text{for} - \end{cases} \qquad \text{(A8)}$$

where for the expression of $\delta\theta_f$, we neglect the nonconservation of θ during mixing because H^D is insensitive to this nonconservation according to (16).

Following the definition of H^D ((11a) and (11d)), and using (A3), (A6)–(A8), we derive

$$H_i^D - H_f^D = \frac{1}{D}\int_{-D}^0 (\delta\theta_i - \delta\theta_f)(-g\alpha_0 z - 0.5g\alpha_z z^2)\mathrm{d}z + \frac{1}{D}\int_{-D}^0 (\delta S_i - \delta S_f)(g\beta z)\mathrm{d}z$$
$$+ \frac{1}{D}\int_{-D}^0 (\delta\theta_i^2 - \delta\theta_f^2)(-g\gamma_{\theta\theta}z)\mathrm{d}z, \qquad \text{(A9)}$$

$$= \left\{ -\frac{1}{3}g\alpha_z\Delta\theta D^2\left[\lambda(\lambda-1)(1-2\lambda) + (2\lambda-3\lambda^2)\frac{D_f}{D} - \lambda^2\frac{D_f^2}{D^2}\right] \right.$$
$$+ \left\{ -\frac{1}{12}N_{\mathrm{WSW}}^2\lambda^3 D^2 - \frac{1}{2}\lambda[(1-\lambda)D - D_f]\frac{\delta\rho}{\rho_0}g \right\}$$
$$\left. + \left\{ 2g\gamma_{\theta\theta}\Delta\theta^2(D+D_f)(\lambda - \frac{\lambda^2 D}{D-D_f}) \right\} \right\}$$
$$\text{(A10)}$$

$$= S_{\mathrm{tb}} - S_{\mathrm{strat}} + S_{\mathrm{cab}}. \qquad \text{(A11)}$$

In (A10), the three brace terms are proportional to thermobaricity (α_z), stratification factors (N_{WSW}^2, $\delta\rho$), and cabbeling coefficient ($\gamma_{\theta\theta}$), respectively. We denote them in (A11) as S_{tb}, $-S_{\mathrm{strat}}$ and S_{cab}, respectively, representing the sinks/sources of H^D related to thermobaricity, stratification and cabbeling. These expressions are consistent with (20a), (21b) and (25) that are based on more physically intuitive derivation. By combining (A11) and (A1), we finally derive (1). Note that $(H_i^D - H_f^D)$ expressed by (A10) is in units of J/kg.

REFERENCES

Adkins, J. F., A. P. Ingersoll, and C. Pasquero, 2005: Rapid climate change and conditional instability of the glacial deep ocean from the thermobaric effect and geothermal heating. *Quat. Sci. Rev.*, **24 (5)**, 581–594.

Akitomo, K., 1999a: Open-ocean deep convection due to thermobaricity: 1. Scaling argument. *J. Geophys. Res.: Oceans*, **104 (C3)**, 5225–5234.

Akitomo, K., 1999b: Open-ocean deep convection due to thermobaricity: 2. Numerical experiments. *J. Geophys. Res.: Oceans*, **104 (C3)**, 5235–5249.

Akitomo, K., 2005: Numerical study of baroclinic instability associated with thermobaric deep convection at high latitudes: Idealized cases. *Deep-Sea Res. Oceanogr., A*, **52 (6)**, 937–957.

Akitomo, K., 2006: Thermobaric deep convection, baroclinic instability, and their roles in vertical heat transport around Maud Rise in the Weddell Sea. *J. Geophys. Res.: Oceans*, **111 (C9)**, C09 027.

Akitomo, K., 2007: Restriction of convective depth in the Weddell Sea. *Geophys. Res. Lett.*, **34 (10)**, L10 610.

Arakawa, A., 1997: Computational design for long-term numerical integration of the equations of fluid motion: two-dimensional incompressible flow. Part I. *J. Comput. Phys.*, **135 (2)**, 103–114.

Arakawa, A. and W. H. Schubert, 1974: Interaction of a cumulus cloud ensemble with the large-scale environment, Part I. *J. Atmos. Sci.*, **31 (3)**, 674–701.

Carmack, E. C., 1979: Combined influence of inflow and lake temperatures on spring circulation in a riverine lake. *J. Phys. Oceanogr.*, **9 (2)**, 422–434.

Carmack, E. C., W. J. Williams, S. L. Zimmermann, and F. A. McLaughlin, 2012: The Arctic Ocean warms from below. *Geophys. Res. Lett.*, **39 (7)**.

Denbo, D. W. and E. D. Skyllingstad, 1996: An ocean large-eddy simulation model with application to deep convection in the Greenland Sea. *J. Geophys. Res.: Oceans*, **101 (C1)**, 1095–1110.

Emanuel, K. A., D. N. J., and C. S. Bretherton, 1994: On large-scale circulations in convecting atmospheres. *Quart. J. Roy. Meteor. Soc.*, **120 (519)**, 1111–1143.

Garwood Jr, R. W., S. M. Isakari, and P. C. Gallacher, 1994: Thermobaric convection. *Geoph. Monog. Series*, **85**, 199–209.

Gill, A. E., 1982: *Atmosphere-Ocean dynamics*, Vol. 30. Academic press.

Gordon, A. L. and B. A. Huber, 1990: Southern Ocean winter mixed layer. *J. Geophys. Res.: Oceans*, **95 (C7)**, 11 655–11 672.

Gregory, D., J. J. Morcrette, C. Jakob, A. C. M. Beljaars, and T. Stockdale, 2000: Revision of convection, radiation and cloud schemes in the ecmwf integrated forecasting system. *Quart. J. Roy. Meteor. Soc.*, **126 (566)**, 1685–1710.

Harcourt, R. R., 1999: Numerical simulation of deep convection and the response of drifters in the Labrador Sea. *Ph.D. thesis, University of California, Santa Cruz, 367 pp.*

Harcourt, R. R., 2005: Thermobaric cabbeling over Maud Rise: Theory and large eddy simulation. *Prog. Oceanogr.*, **67 (1)**, 186–244.

Harcourt, R. R. and E. A. D'Asaro, 2008: Large-eddy simulation of Langmuir turbulence in pure wind seas. *J. Phys. Oceanogr.*, **38 (7)**, 1542–1562.

Harcourt, R. R., E. L. Steffen, R. W. Garwood, and E. A. D'Asaro, 2002: Fully Lagrangian floats in Labrador Sea deep convection: Comparison of numerical and experimental results. *J. Phys. Oceanogr.*, **32 (2)**, 493–510.

Huang, R. X., 2014: Energetics of lateral eddy diffusion/advection: Part I. Thermodynamics and energetics of vertical eddy diffusion. *Acta Oceanol. Sin.*, **33 (3)**, 1–18.

Ingersoll, A. P., 2005: Boussinesq and anelastic approximations revisited: Potential energy release during thermobaric instability. *J. Phys. Oceanogr.*, **35 (8)**, 1359–1369.

IOC, SCOR, and IAPSO, 2010: *The International Thermodynamic Equations of Seawater-2010: Calculation and Use of Thermodynamic Properties.* Intergovernmental Oceanographic Commission, Manuals and Guides, UNESCO.

Jackett, D. R., T. J. McDougall, R. Feistel, D. G. Wright, and S. M. Griffies, 2006: Algorithms for Density, Potential Temperature, Conservative Temperature, and the Freezing Temperature of Seawater. *J. Atmos. Oceanic Technol.*, **23 (12)**, 1709–1728.

Jones, H. and J. Marshall, 1997: Restratification after deep convection. *J. Phys. Oceanogr.*, **27 (10)**, 2276–2287.

Landau, L. D. and E. M. Lifshitz, 1959: *Fluid mechanics.* Pergamon Press.

Large, W. G., J. C. McWilliams, and S. C. Doney, 1994: Oceanic vertical mixing: A review and a model with a nonlocal boundary layer parameterization. *Rev. Geophys.*, **32 (4)**, 363–403.

McDougall, T. J., 1987: Thermobaricity, cabbeling, and water-mass conversion. *J. Geophys. Res.: Oceans*, **92 (C5)**, 5448–5464.

McDougall, T. J., 2003: Potential enthalpy: A conservative oceanic variable for evaluating heat content and heat fluxes. *J. Phys. Oceanogr.*, **33 (5)**, 945–963.

McPhee, M. G., 2000: Marginal thermobaric stability in the ice-covered upper ocean over Maud Rise. *J. Phys. Oceanogr.*, **30 (11)**, 2710–2722.

McPhee, M. G., 2003: Is thermobaricity a major factor in Southern Ocean ventilation? *Antarct. Sci.*, **15 (01)**, 153–160.

McPhee, M. G., et al., 1996: The antarctic zone flux experiment. *Bull. Amer. Meteor. Soc.*, **77 (6)**, 1221–1232.

Padman, L., R. Muench, and E. Fahrbach, 1998: Cabbeling catastrophes. *J. Geophys. Res.: Oceans*, submitted.

Press, W. H., 2007: *Numerical recipes 3rd edition: The art of scientific computing.* Cambridge university press.

Radko, T., A. Bulters, J. D. Flanagan, and J.-M. Campin, 2014: Double-diffusive recipes. Part I: Large-scale dynamics of thermohaline staircases. *J. Phys. Oceanogr.*, **44 (5)**, 1269–1284.

Reddy, J. N., 2002: *Energy Principles and Variational Methods in Applied Mechanics.* John Wiley & Sons.

Schmid, M., N. M. Budnev, N. G. Granin, M. Sturm, M. Schurter, and A. Wüest, 2008: Lake baikal deepwater renewal mystery solved. *Geophys. Res. Lett.*, **35 (9)**.

Su, Z., A. P. Ingersoll, A. L. Stewart, and A. F. Thompson, 2015: Ocean Convective Available Potential Energy. Part I: Concept and Calculation. *J. Phys. Oceanogr.*, submitted.

Trenberth, K., 2005: Uncertainty in Hurricanes and Global Warming. *Science*, **308 (5729)**, 1753–1754.

Turner, J. S., 1979: *Buoyancy effects in fluids.* Cambridge University Press.

Vallis, G. K., 2006: *Atmospheric and Oceanic Fluid Dynamics: Fundamentals and Large-Scale Circulation.* Cambridge University Press.

Weiss, R. F., E. C. Carmack, and V. M. Koropalov, 1991: Deep-water renewal and biological production in Lake Baikal. *Nature*, **349 (6311)**, 665–669.

Young, W. R., 2010: Dynamic Enthalpy, Conservative Temperature, and the Seawater Boussinesq Approximation. *J. Phys. Oceanogr.*, **40 (2)**, 394–400.

Zhang, G. J., 2009: Effects of entrainment on convective available potential energy and closure assumptions in convection parameterization. *J. Geophys. Res.: Atmos.*, **114 (D7)**.